Title

Multiphoton Magnetic Resonance Imaging

Author

Han, Victor

Publication Date

2022

Peer reviewed|Thesis/dissertation

Multiphoton Magnetic Resonance Imaging

by

Victor Han

A dissertation submitted in partial satisfaction of the

requirements for the degree of

Doctor of Philosophy

in

Engineering - Electrical Engineering and Computer Sciences

in the

Graduate Division

of the

University of California, Berkeley

Committee in charge:

Professor Chunlei Liu, Chair
Professor Michael Lustig
Associate Professor Moriel Vandsburger

Spring 2022

Multiphoton Magnetic Resonance Imaging

Abstract

Multiphoton Magnetic Resonance Imaging

by

Victor Han

Doctor of Philosophy in Engineering - Electrical Engineering and Computer Sciences

University of California, Berkeley

Professor Chunlei Liu, Chair

Magnetic resonance imaging (MRI) consists of three main components: a main static magnetic field for producing magnetization in a sample or subject, spatially varying magnetic fields for spatial encoding of the magnetization, and radiofrequency (RF) magnetic fields for manipulating the magnetization. This dissertation is mainly concerned with the RF fields. The frequency of the RF fields is set to the resonance determined by the strength of the main magnetic field and the properties of the object being imaged. For the usual case of imaging Hydrogen nuclei, the frequency is on the order of hundreds of MHz on superconducting clinical MRI scanners. While standard MRI only uses RF near the resonance frequency, we propose the use of multiphoton excitation in MRI, where multiple RF fields whose frequency sums or differences equal the resonance frequency are used instead. No RF at the resonance frequency is required.

We begin by verifying multiphoton resonances in MRI via simulation and experiment. Practically, this is done using a combination of RF in the kHz and RF in the MHz, for example 30 kHz and 127.71 MHz for a 127.74 MHz resonance frequency. While multiphoton excitation with RF at a single subharmonic frequency, such as with half-resonance frequency RF at 63.87 MHz for a 127.74 MHz resonance, is possible, it is not practical for human scale MRI due to excessive power requirements. Although the RF fields in MRI are often praised for being safe in that they are non-ionizing, they still pose the danger of potentially excessively heating a subject.

By using RF in the kHz and the MHz, the power efficiency of multiphoton excitation is greatly increased, and the kHz RF provides negligible additional power deposition in the human body. By taking advantage of this fact, we can actually reduce overall power deposition in the body in more spatially complex excitation patterns such as multiband excitation by simultaneously making use of multiple multiphoton resonance conditions at different spatial locations. With the addition of power-deposition-negligible kHz RF, the power-deposition

intensive MHz RF can be reused for multiple excitations at different spatial locations instead of just one spatial location.

Next we move onto providing a more rigorous analysis of spatially selective excitation with multiphoton resonances. With this analysis we see that amplitude and frequency modulation can be traded-off between the different RF fields in a multiphoton resonance, granting additional flexibility. After demonstrating this additional flexibility with a homemade extra kHz-range RF coil, we also show its practicality on an in vivo human head. As future MRI systems increasingly gain complexity, we believe this additional flexibility will enable novel applications.

To the people who made me who I am today.

Contents

List of Figures

List of Tables

Acknowledgments

I have lived a blessed life, free from hunger, poverty, and major misfortune. For this, I thank my family. Throughout my life, they have provided me with an environment where I could focus on my studies and to not have the fear of failure, for if I did terribly fail, they would catch me. It is thanks to them that I was able to pursue a PhD.

For my PhD studies, I would like to thank Chunlei Liu for being a wonderful advisor. Before coming to Berkeley, I knew nothing about MRI. After taking his brain imaging class in my first semester, I was extremely fortunate that Chunlei accepted me into his lab, despite saying something along the lines of "this is unexpected" when I suddenly asked to join one day. Throughout my graduate studies, I really appreciate the freedom he has given me. He has allowed me to learn whatever interests me and to try my various naive ideas and to usually fail with them, but learning along the way. When I am lost or clueless on how to proceed, he is also always there to provide advice, and ultimately, this dissertation is what emerged from that advice. He is extremely skilled at staying still as a volunteer in long MRI scans and works tirelessly to ensure that funding is not a worry for his students. I couldn't have asked for a better advisor.

Within the lab group, thanks to Jingjia for being a great collaborator. She is witty, creative, and a pleasure to be around. Although the projects we have worked on together have not borne much fruit, I hope that one day there will be something to show for it. For the beginning of my PhD, thanks to Yuyao and Hongjiang for letting me third wheel them at lunch, where they taught me about the world of research and shared their thoughts and beliefs with me. Although our overlap time was relatively short, they made my early days in the lab very welcoming and joyful. Thanks to Miriam for her endless positivity, for making great guacamole, for helping with anything wet-lab related, and for complimenting my RF coils no matter how unpolished they were. She is immensely helpful in providing samples to do MRI scans on and I'm glad that I was able to help her with her research. Thanks to Sang Min for being the senior grad student and showing that PhDs can end. Thanks to the newer lab members Zoe, Maruf, Shafeeq, Lexi, Paul, and Engin for the occasional chats inside and outside the lab. Thanks to Tanya for being a great mentee and carrying on multiphoton MRI work, and thanks to Koyam for his easygoing personality and for, like Miriam, appreciating my RF coils. I would also like to thank the more transient members of our lab group. Xiaojun showed me the value of hard work. He would almost always be working, and his results showed it. Despite his hardworking nature, he would always be full of smiles and laughter. Arman was my first undergraduate mentee. Thanks to Arman for being so kind and mature, and for putting up with an inexperienced mentor. Thanks to Neelesh, Kevin, and Sunay for exploring EEG and NMR in the Earth's magnetic field with me, making the work much more enjoyable than if I were alone. Thanks to Eric for being a weeb like me. Thanks to Jianshu for doing a lot of the dirty work I did not want to do and for having great intuition on mechanical design. Thanks to Steven for being so accomplished and yet still saying hi every once in a while.

Although not officially a part of it, I consider Miki Lustig's group to be my second adoptive lab group. Miki is extremely generous with resources and lab space, allowing me to share them with his students. Over the years, Miki and his group members have helped me out in many ways. Thanks to Karthik Gopalan for sharing his immense knowledge on MRI coils, mechanical tools, and a bit of pretty much everything else. I feel I owe a great debt to him that I'm not sure how to repay. Thanks to Anita Flynn for all of her wonderful documentation for passing down knowledge, for having all these great ideas for improving lab spaces, and for actually implementing them. Thanks to Jon Tamir for setting me up with computing server accounts and using the wrist MRI scanner. Thanks to Jim Tropp for teaching me the fundamentals of coil design for MRI. Thanks to Ekin Karasan for introducing me to Heartvista and for being the one to gather everyone together. Thanks to Ke Wang, Alfredo De Goyeneche, and Alan Dong for maintaining computing resources. Thanks to Julian Maravilla for many enthusiastic chats about coils. Thanks to Shreya Ramachandran for her help with BART. Thanks to Rahul Tewari for his humor. And of course, thanks to Miki for all of his advice, his welcoming attitude, and his uncompromising attitude on safety.

Thanks to Moriel Vandsburger for both being in my committee and having me on the teaching team for BioE 105 two years in a row. Moriel is very chill and kind. It was a pleasure working with you.

Outside of work, thanks to Ellis Ratner for being my most consistent tennis buddy. I've had many tennis buddies, but they don't usually last so many years. Thanks to Jingwei Shi for being my friend through undergrad and then being my Stanford buddy. Thanks to Sung Hoon Choi for helping me get an iPhone with an employee discount. Thanks to Efe Aras for teaching me how to wrestle. Thanks to Andrew Chen and Andrew Ho for taking me on amazing camping and backpacking adventures and for cooking delicious meals. Thanks to Andrew Wang for letting me live in his attic when I didn't have a place to stay. Thanks to Jingjia for providing emotional support at a time I needed it the most. Thanks to my San Diego friends for the occasional chats and online video games. We have all taken very different paths in life but I still feel very connected to you all.

Finally, I'd like to thank Hansheng. Hansheng kept me sane during COVID stay-at-home orders. We survived the pandemic and the majority of grad school together. Thanks for making life a joy.

Chapter 1

Introduction

1.1 Magnetic Resonance Imaging

The human body is full of tiny magnets. Magnetic resonance imaging (MRI) manipulates and probes these magnets in order to form an image. Although there are many potential magnets to choose from such as unpaired electrons, ^{13}C nuclei, and ^{23}Na nuclei, most MRI is performed with ^{1}H nuclei. It's no wonder since a quick order-of-magnitude calculation tells us that there are around 10^{26} ^{1}H nuclei in the human body.

As the name magnetic resonance implies, each type of magnet, often called a spin, has a resonance frequency when placed in another magnetic field. For nuclear ^{1}H spins, the resonance frequency is about 127.74 MHz when placed in an external 3 Tesla (3 T) magnetic field, as determined by the constant of proportionality, called the gyromagnetic ratio, of 42.58 MHz/T for ^{1}H spins. This 127.74 MHz resonance frequency is also known as the Larmor frequency. When radiofrequency (RF) magnetic fields at the Larmor frequency are supplied to the spins in the external magnetic field, the spins can be manipulated to transition between quantum mechanical energy eigenstates, or more generally enter new superpositions of energy eigenstates. Geometrically, if a vector pointing upwards represents a lower energy eigenstate and a vector pointing downwards represents an upper energy eigenstate, then any vector pointing in a different direction represents a superposition of the two energy eigenstates. When there are many spins acting together on a macroscopic scale, essentially the same picture applies. Resonant RF fields are able to manipulate the total magnetization vector composed of many spins to anywhere on the surface of the sphere formed by arbitrary vector directions, and the equations that govern motion on the sphere are the Bloch equations. Once the magnetization vector is excited away from the z-axis, it can be probed and an image can be formed.

This dissertation is concerned with excitation in MRI. Specifically, we explore the fact that instead of just using a single RF field at the Larmor frequency to produce excitation, we can also use multiple RF fields all far from the Larmor frequency to cooperatively produce excitation. These fields produce excitation when more general multiphoton resonance

conditions are met.

1.2 Dissertation Organization

The remainder of this dissertation is organized as follows. Chapter 2 introduces multiphoton resonances in MRI. Chapter 3 describes Bloch equation simulations for verifying multiphoton resonances. Chapter 4 describes experiments for verifying multiphoton resonances. Chapter 5 goes more in-depth into the theory, providing derivations for spatially selective excitation in a more rigorous manner. Chapter 6 utilizes the theory from chapter 5 to demonstrate the flexibility that multiphoton excitation provides in that multiphoton excitation allows for the same excitation to be produced in a variety of ways. Chapter 7 describes the results of in vivo MR images produced using multiphoton excitation. Chapter 8 describes preliminary work applying multiphoton excitation to excitation in the Earth's magnetic field. Chapter 9 discusses future work and conclusions. Chapter 10 is an appendix with details for some derivations and definitions for variables used throughout the dissertation. Please see chapter 10 when variables such as B_0, etc are undefined.

Chapter 2

Multiphoton Resonance Introduction

Today's MRI assumes one-photon excitation [25]. That is, for each nuclear spin, one photon accompanies the transition between energy states. This photon must resonate near the Larmor frequency. Here, we show that, instead of the usual one-photon resonance, we can excite multiphoton resonances to generate signal for MRI by using multiple magnetic field frequencies, none of which is near the Larmor frequency. Only the total energy absorbed by a spin must correspond to the Larmor frequency. One frequency must still be relatively close to the Larmor frequency, however, to avoid needing extremely high intensity fields and allow for practicality in imaging. Although virtual photons instead of real photons usually contribute more to signal [19], we will use terms absorption and emission in this dissertation.

Multiphoton excitation has been described for nuclear magnetic resonance (NMR) [31, 12, 11, 46, 5, 1] and electron paramagnetic resonance (EPR) [16, 39]. For NMR, two-photon excitation has been used to permit simultaneous RF transmit and receive, as the transmitted RF has distinctive frequency from received RF tuned at the Larmor frequency. For continuous-wave EPR, B_0 modulation has been recast into a multiphoton excitation framework, where multiple photons polarized in the z-direction parallel to B_0 generate excitation together with a single photon polarized in the xy-plane. For MRI, however, multiphoton excitation has not yet been well explored. The idea that oscillating z-direction magnetic fields creates frequency "sidebands" is well known and has been used occasionally, both in excitation [7] and reception [40]. For excitation, it was used for simultaneous transmit and receive, and for reception, it was used to accelerate spatial information acquisition by increasing the receive bandwidth. However, as we will show, a multiphoton framework using Bloch equations and rotating frame transformations makes it clear that these multiphoton excitations excite extra resonances that look just like one-photon resonances, and concepts such as the Bloch-Siegert (BS) shift, slice selective excitation, and adiabatic RF pulses readily generalize.

Although we describe an effect that is quantum mechanical in name and in nature, the entirety of the analysis in this dissertation will be in a classical framework. We provide a completely geometrical interpretation of multiphoton effects.

2.1 Basic Spin Physics

When placed in an external magnetic field, spins precess around that magnetic field. The precessional motion can be visualized as a dreidel or other spinning top. When aligned vertically with the external magnetic field, spins stay put. When tilted away from the vertical, the spins move circularly around the vertical. A spinning bicycle wheel on a string is another great example to search for videos of. For spins in MRI, the precessional motion frequency, also known as the Larmor frequency, is equal to γB_0, which is the gyromagnetic ratio γ multiplied by the main magnetic field strength B_0.

2.1.1 Resonances

The precessional motion frequency or Larmor frequency is also the resonance frequency. When magnetic fields at the Larmor frequency are applied to the spins in the xy-plane, the angle that the spins make with B_0, traditionally said to be in the z-direction, can change. This change in angle is called nutation. Much like how pushes to a child on a swing should be in sync with the swing to produce sizeable changes, RF magnetic fields should also be in sync with the Larmor frequency precession to produce excitation.

2.1.2 Rotating Frames

To more clearly see the effect of resonant excitation, instead of viewing things from the "laboratory frame," we can move with the spins' precession. If we rotate our frame of reference aorund the z-axis at the Larmor frequency, then the spins appear to be stationary even when tilted away from B_0. To make our equations of motion still valid, because there is no precession in this frame of reference, then there must not be any magnetic field! By taking the rotating frame of reference, we have introduced a new fictitious z-axis magnetic field that cancels out our B_0 field from the laboratory frame. More generally, if we rotated our frame of reference not at the Larmor frequency, but at some offset frequency, then we would not have full cancellation of the B_0 field, and the spins would still be precessing at the frequency expected based on our rotating frame's rotation frequency relative to the Larmor frequency.

Rotating frames make the analysis of simple RF pulses easy. If the RF pulse is at the Larmor frequency, then in the Larmor frequency rotating frame, the magnetic field from the RF pulse is stationary. Since it is the only magnetic field, because the B_0 was cancelled out, the spins precess around the stationary RF magnetic field (Fig. 2.1b). The stationary RF magnetic field is in the xy-plane, so if the spins begin along the z-axis, they nutate from the z-axis to the xy-plane, to the negative z-axis, to the xy-plane, and back to the positive z-axis. If the RF pulse ends when the spins are in the xy-plane, then the RF pulse is said to be a 90° pulse and signal can be acquired as the spins precess.

If the RF pulse is not at the Larmor frequency, then in the Larmor frequency rotating frame, the magnetic field is not stationary and unless the magnetic field is much stronger

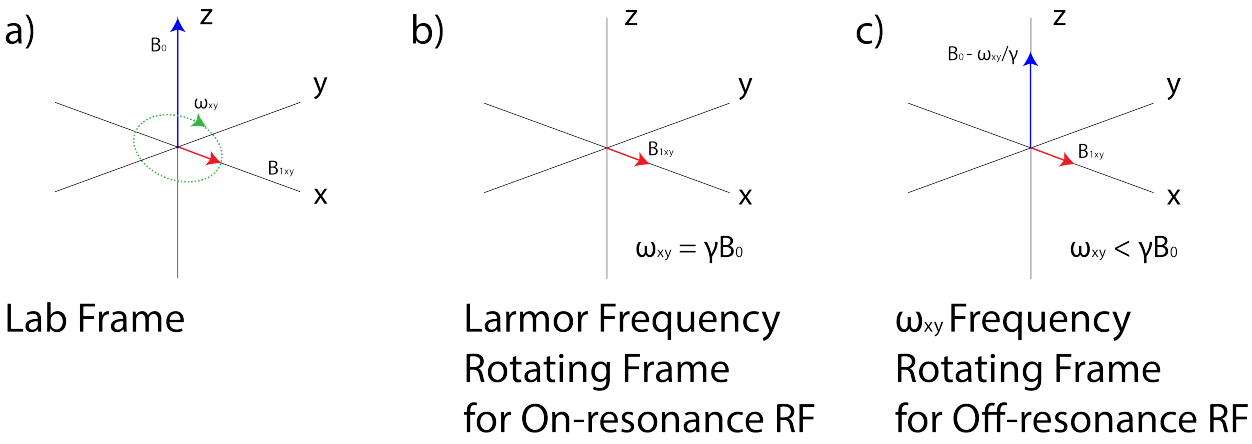

Figure 2.1: **Rotating frames.** a) A main magnetic field and a circularly polarized RF field in the laboratory frame of reference. b) When the RF is at the Larmor frequency, the Larmor frequency rotating frame only has a stationary field in the xy-plane. c) When the RF is not at the Larmor frequency, a rotating frame at the RF frequency shows a stationary magnetic field that is easily dominated by the z-axis field, depending on the strength of the RF field and the offset from the Larmor frequency.

than its frequency, the spins do not do much nutation. To view this differently, we can take a rotating frame at the RF frequency instead. If the RF pulse is not at the Larmor frequency, then there will be a residual z-axis magnetic field and a stationary xy-plane field from the RF in this rotating frame. The spins then precess around the total magnetic field. If the RF field is small compared to the offset from the Larmor frequency, then the total magnetic field is approximately along the z-axis and no nutation/excitation occurs (Fig. 2.1c).

2.1.3 Selective Excitation

When imaging with magnetic resonance, a magnetic field gradient along the z-axis is used to make the Larmor frequency vary with space. By providing a RF pulse with a limited bandwidth, only the spatial location with a matching local Larmor frequency is excited (Fig. 2.2). The RF pulse is usually amplitude modulated to achieve the desired excitation profile.

2.2 Multiphoton Resonance Theory

Standard one-photon excitation occurs when the RF field (B_1) is polarized in the xy-plane, perpendicular to the main magnetic field B_0. A variant of multiphoton effects occurs when

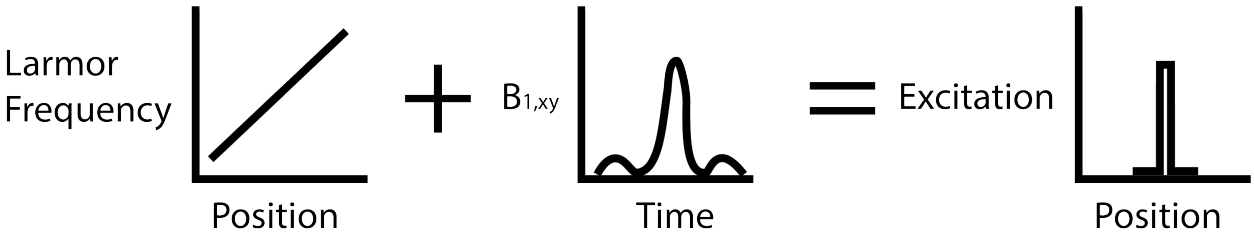

Figure 2.2: **Slice-selective excitation.** When imaging with magnetic resonance, a magnetic field gradient along the z-axis is used to make the Larmor frequency vary with space. By providing a RF pulse with a limited bandwidth, only the spatial location with a matching local Larmor frequency is excited.

we add more RF fields along the z-axis, parallel to the main magnetic field B_0. The term RF is used very loosely to include any oscillation frequency. Although it is also possible to have multiphoton effects with RF only in the xy-plane [46], the effects for our pulse durations were not practical for generating reasonable flip angles and for avoiding overlap with one-photon excitation, so we will not consider them here.

2.3 Two-Photon Excitation

2.3.1 Phase-modulated Rotating Frame

Consider two B_1 fields with frequencies ω_{xy} and ω_z along the xy-plane and z-axis respectively. The total magnetic field in the laboratory frame is

$$B_z = B_0 + B_{1,z}\cos(\omega_z t) \tag{2.1}$$

$$B_x = B_{1,xy}\cos(\omega_{xy} t) \tag{2.2}$$

$$B_y = -B_{1,xy}\sin(\omega_{xy} t) \tag{2.3}$$

where the RF field in the xy-plane is clockwise circularly polarized; $B_{1,xy}$ and $B_{1,z}$ are amplitudes of each RF field. In a clockwise rotating frame with an angular velocity of ω_{rot}, the effective B_z field is

$$B_{z,eff} = B_z - \omega_{rot}/\gamma \tag{2.4}$$

To generate time-invariant $B_{z,eff}$, we choose

$$\omega_{rot} = \omega_{xy} + \gamma B_{1,z}\cos(\omega_z t) \tag{2.5}$$

We refer this rotating frame as the phase-modulated rotating frame following [31]. This choice of ω_{rot} results in a non-stationary xy-plane RF field. To illustrate this effect, we examine the phase accrual of the xy-RF field in the rotating frame. Let θ be the phase, then

$$B_{x,eff} = B_{1,xy}\cos(\theta) \tag{2.6}$$

$$B_{y,eff} = B_{1,xy}\sin(\theta) \tag{2.7}$$

By definition,

$$\theta = \int_0^t (\omega_{rot} - \omega_{xy})dt = \frac{\gamma B_{1,z}}{\omega_z}\sin(\omega_z t) \tag{2.8}$$

Combining Eqs. [2.4-2.8] gives

$$B_{z,eff} = B_0 - \frac{\omega_{xy}}{\gamma} \tag{2.9}$$

$$B_{x,eff} = B_{1,xy}\cos\left(\frac{\gamma B_{1,z}}{\omega_z}\sin(\omega_z t)\right) \tag{2.10}$$

$$B_{y,eff} = B_{1,xy}\sin\left(\frac{\gamma B_{1,z}}{\omega_z}\sin(\omega_z t)\right) \tag{2.11}$$

2.3.2 Resonance Conditions

Eqs. [2.10, 2.11] can be Taylor expanded if $\frac{\gamma B_{1,z}}{\omega_z} \ll 1$ as

$$B_{x,eff} \approx B_{1,xy} \tag{2.12}$$

$$B_{y,eff} \approx B_{1,xy}\frac{\gamma B_{1,z}}{\omega_z}sin(\omega_z t) \tag{2.13}$$

From Eqs. [2.9, 2.12, 2.13], three potential resonances exist depending on the relative values of the frequencies (Fig. 2.3).

- One-photon resonance: If $\omega_{xy} = \gamma B_0$, then $B_{z,eff} = 0$ and $B_{x,eff}$ tilts magnetization from the z-axis. This is the normal on-resonance condition.
- Two-photon resonances: If $\omega_{xy} = \gamma B_0 \pm \omega_z$, then $B_{z,eff} = \mp\omega_z/\gamma$. The linearly polarized RF field $B_{y,eff}$ oscillates with an angular frequency of ω_z, matching the amplitude of $B_{z,eff}$, which induces resonances. These two new resonances correspond to state transitions where a single xy-polarized photon is absorbed and a single z-polarized photon is absorbed or emitted, depending on whether the xy-frequency is below or above the Larmor frequency. From Eq. [2.13], just like with single photon excitation, by taking another rotating frame with angular velocity $\mp\omega_z$ and dividing the $B_{y,eff}$ amplitude by 2 for only one circularly polarized component, in agreement with prior work, the effective angular nutation frequency for two-photon excitation is

$$\omega_{nut} = \frac{\gamma B_{1,xy}\gamma B_{1,z}}{2\omega_z} \tag{2.14}$$

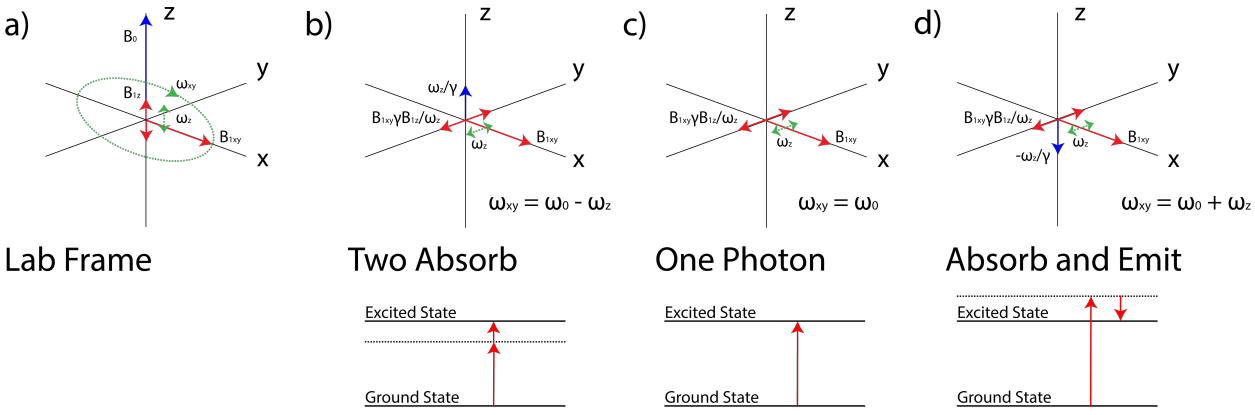

Figure 2.3: **One- and two-photon excitation conditions.** a) Magnetic field setup in the laboratory frame with arbitrary frequencies for the xy- and z-RF fields. b) In the phase-modulated rotating frame with $\omega_{xy} = \gamma B_0 - \omega_z$, there is a remaining static z-field that resonates with the oscillating field on the y-axis. In this case, both a xy- and z-photon are absorbed. c) In the phase-modulated rotating frame with $\omega_{xy} = \gamma B_0$, there is no remaining static z-field, and the static x-field causes the resonance. This is the standard one-photon resonance. d) In the phase-modulated rotating frame with $\omega_{xy} = \gamma B_0 + \omega_z$, there is a remaining static z-field that resonates with the oscillating field on the y-axis. In this case, a xy-photon is absorbed while a z-photon is emitted.

Until this point, we have essentially followed the classical approach of Eles and Michal [11] with two differences: arbitrary frequencies and separated $B_{1,xy}$ and $B_{1,z}$ fields.

2.3.3 Multiphoton Excitation

If more terms are kept in the Taylor expansion of Eqs. [2.10, 2.11], we can analyze higher-order excitations with three or more photons. However, Taylor expansion requires $\frac{\gamma B_{1,z}}{\omega_z} \ll 1$. Alternatively, we can exactly expand $B_{x,eff}$ and $B_{y,eff}$ using Bessel functions (Chapter 10: Appendix), which reveals that for any integer n, resonance occurs whenever

$$\omega_{xy} = \gamma \ B_0 + n\omega_z \tag{2.15}$$

and for each integer n, the corresponding effective angular nutation frequency is

$$\omega_{nut} = \gamma \ B_{1,xy} J_n \left(\frac{\gamma B_{1,z}}{\omega_z} \right) \tag{2.16}$$

J_n represents the Bessel function of the first kind of order n. n represents the number of z-axis photons in the resonance. As the maximum of Bessel functions occurs at gradually

$\gamma B_{1,z}/\omega_z$	J_0	J_1	J_2	J_3	J_4	J_5
0.00	1.00	0.00	0.00	0.00	0.00	0.00
0.50	0.94	0.24	0.03	0.00	0.00	0.00
1.00	0.77	0.44	0.11	0.02	0.00	0.00
1.50	0.51	0.56	0.23	0.06	0.01	0.00
2.00	0.22	0.58	0.35	0.13	0.03	0.01
2.41	0.00	0.52	0.43	0.20	0.07	0.02
3.00	-0.26	0.34	0.49	0.31	0.13	0.04
4.00	-0.40	-0.07	0.36	0.43	0.28	0.13
4.50	-0.32	-0.23	0.22	0.42	0.35	0.19
5.52	0.00	-0.34	-0.12	0.25	0.40	0.32

Table 2.1: Example Bessel function values. Note that as the ratio of z-axis RF strength to frequency increases, higher order multiphoton effects start to become non-negligible. Also note that multiphoton efficiencies oscillate with the ratio, and that the zero crossings of Bessel function are not quite periodic.

larger arguments for higher orders, larger $\frac{\gamma B_{1,z}}{\omega_z}$ is needed to generate multiphoton resonances. Generalizing further, if we have photons of different frequencies along the z-axis, we simply multiply another Bessel function for that frequency (Chapter 10: Appendix). In the case of two different frequencies, we have resonances whenever

$$\omega_{xy} = \gamma\ B_0 + n\omega_{z1} + m\omega_{z2} \tag{2.17}$$

and for each n and m, the corresponding angular nutation frequency is given by

$$\omega_{nut} = \gamma\ B_{1,xy} J_n\left(\frac{\gamma B_{1,z1}}{\omega_{z1}}\right) J_m\left(\frac{\gamma B_{1,z2}}{\omega_{z2}}\right) \tag{2.18}$$

As a side note, Bessel function expansion has also been used in the context of excitation k-space with sinusoidal gradient waveforms [37, 29].

2.3.4 Bloch-Siegert Shift

Off-resonance RF fields slightly shift resonance frequencies, a phenomenon termed the Bloch-Siegert shift [4, 38]. This shift also affects multiphoton excitation, as off-resonant RF fields are always employed. The resulting BS-shifts can be calculated based on all the off-resonant terms in the phase-modulated rotating frame. Specifically, each off-resonant term adds a BS-shift. To the second order, the BS-shift is

$$\omega_{BS} = \frac{\left(\gamma B_{1,off}\right)^2}{2\omega_{off}} \tag{2.19}$$

where $B_{1,off}$ is the magnitude of the off-resonant RF field and ω_{off} is the frequency offset from the resonance, which can be a single-photon resonance or any multiphoton resonance. In theory, the number of off-resonant terms, whose amplitudes are given by the integer orders of the Bessel function, will be infinite. The infinite sums can be approximated by the Carson's bandwidth rule [9], which heuristically states that approximately 98% of the power of a frequency-modulated signal will be contained in a bandwidth of $2\left(\beta+1\right)B$, where β is the peak modulation index and B is the highest frequency in the modulating signal. In our case, β is the largest $\frac{\gamma B_{1,zn}}{\omega_{zn}}$ and B is the largest ω_{zn}.

Consider a case with one $B_{1,xy}$ and two $B_{1,z}$, where resonances occur at $\omega_{xy} = \gamma B_0 + k\omega_{z1} + l\omega_{z2}$. Then, the off-resonant terms in the phase-modulated rotating frame are (Chapter 10: Appendix, Eq. [10.15])

$$B_{xy,off} = B_{1,xy} \sum_{(n,m)\neq(k,l)} J_n\left(\frac{\gamma B_{1,z1}}{\omega_{z1}}\right) J_m\left(\frac{\gamma B_{1,z2}}{\omega_{z2}}\right) e^{i((n-k)\omega_{z1}+(m-l)\omega_{z2})} \tag{2.20}$$

Each of these terms contributes to the BS-shift as approximated by Eq. [2.19], resulting in a total BS-shift of

$$\omega_{BS\ total} = \frac{\left(\gamma B_{1,xy}\right)^2}{2} \sum_{(n,m)\neq(k,l)} \frac{\left(J_n\left(\frac{\gamma B_{1,z1}}{\omega_{z1}}\right) J_m\left(\frac{\gamma B_{1,z2}}{\omega_{z2}}\right)\right)^2}{\left(n-k\right)\omega_{z1} + \left(m-l\right)\omega_{z2}} \tag{2.21}$$

The summation can be evaluated numerically with Carson's bandwidth rule.

Chapter 3

Multiphoton Resonance Simulations

In the previous chapter, we used rotating frames to determine multiphoton resonance conditions. In this chapter, we verify the resonances described in the previous chapter via simulation. A deep understanding of the Bloch equations is not needed to understand the simulation results, so the actual equations will be introduced in a later chapter.

3.1 Methods

3.1.1 Numerical Simulation

Bloch equation simulations were performed in Matlab R2017a (MathWorks,Inc., Natick, MA) using the built-in ode45 or ode113 solver. All xy-frequencies represent offsets from the Larmor frequency, as we used the rotating frame at the Larmor frequency.

3.1.2 Resonance Verification

Firstly, multiphoton resonances were verified by evaluating resulting transverse magnetization versus various combinations of xy- and z-RF frequencies (10-ms hard pulses). RF in xy and z were swept from -30 kHz to 30 kHz and from 0 to 30 kHz with a step size of 60 and 30 Hz, respectively. For each simulated point, $B_{1,z}$ was chosen such that $\frac{\gamma B_{1,z}}{\omega_z} = 1$. $B_{1,xy}$ was kept at a constant 1 μT.

3.1.3 Nutation Frequency Verification

Simulation was then compared with the analytical nutation frequency expressions over a wide range of magnetic field strengths and frequencies that may be encountered in practice. Because the analytical expressions give resonance nutation frequencies, simulation must consider the BS-shift as described in Chapter 2. For example, if a two-photon resonance is desired with $\omega_{xy} = \omega_0 + 10000$ rad/s and $\omega_z = 10000$ rad/s, and it was predicted that the BS-shift was +87 rad/s for this resonance, then the xy-frequency was shifted by the BS-shift such that we

still hit the desired resonance. That is, for the simulation, the frequencies $\omega_{xy} = \omega_0 + 10087$ rad/s and $\omega_z = 10000$ rad/s would be used instead. Analytical transverse magnetizations were calculated using an effective flip angle obtained by multiplying the effective nutation frequency with the hard pulse duration of 10 ms.

3.2 Results

3.2.1 Resonance Verification

The transverse magnetization generated by two perpendicular B_1 pulses ($B_{1,xy}$ and $B_{1,z}$) showed five lines of elevated intensity vs. the 2D frequency sweep (Fig. 3.1a). The center brightest line, corresponding to $\Delta\omega_{xy} = 0$, represents the single-photon resonance. The two lines closest to the center line represent the two-photon resonances, where $\Delta\omega_{xy} \approx \pm\omega_z$. The two furthest lines represent the three-photon resonances, where $\Delta\omega_{xy} \approx \pm 2\omega_z$. Note that with the fixed ratio of $\frac{\gamma B_{1,z}}{\omega_z} = 1$, the excitation efficiency decreases towards higher-order resonances. To further illustrate the multiphoton-resonance nature, Fig. 3.1b&c show representative time and frequency domain plots of a two-photon excitation. Note that there is no component of the excitation at the Larmor frequency. Visualization of magnetization nutation is available in the Supporting Information Videos of [17].

3.2.2 Nutation Frequency Verification

Without BS-shift compensation, there was significant deviation between Bloch simulation and transverse magnetization derived analytically from Eq. [2.16], especially at higher $B_{1,xy}$ strengths (Fig. 3.2d-f). However, with the pre-compensation, the simulation matches nearly exactly the analytical expressions (Fig. 3.2a-c). The effective flip angle increases linearly with the strength of $B_{1,xy}$ (Fig. 3.2a), but changes nonlinearly with increasing $B_{1,z}$ and ω_z, as $J_1\left(\frac{\gamma B_{1,z}}{\omega_z}\right)$ oscillates nonperiodically (Fig. 3.2b&c). Potential deviations between simulation and analytical expressions may occur when the BS-shift approximation is not accurate. The second-order BS-shift approximation used here, however, works well for the range of values shown. While the amplitude of $B_{1,xy}$ has the strongest effect, all parameters influence the BS-shift.

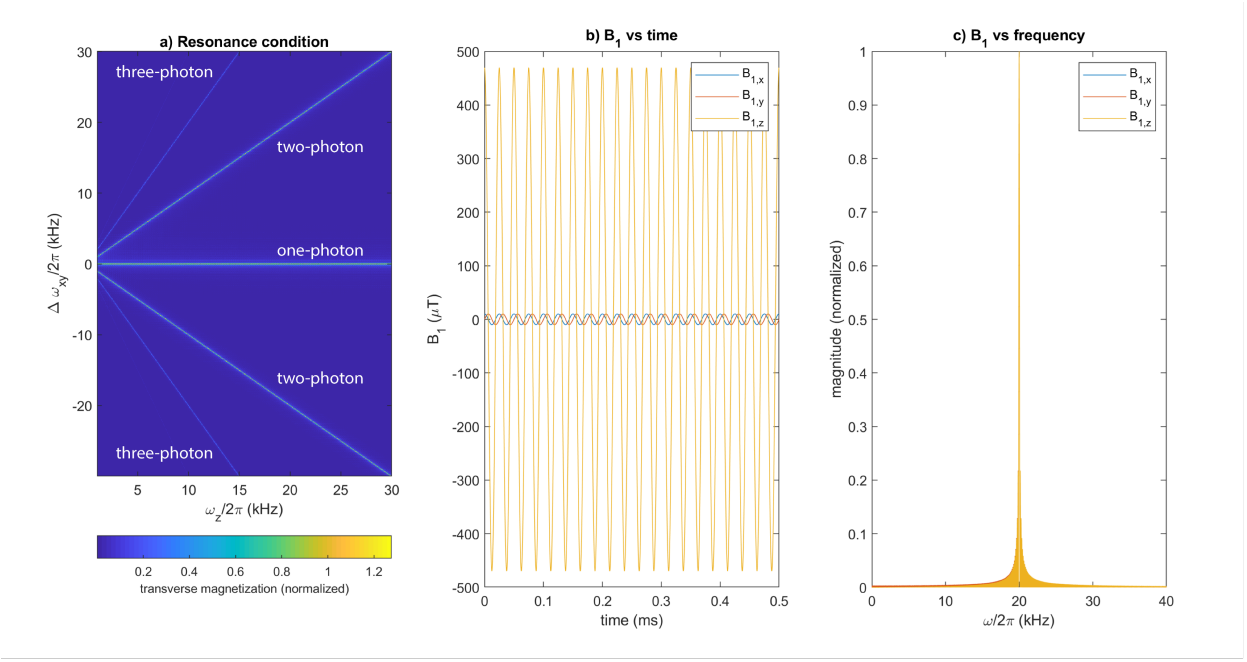

Figure 3.1: **Multiphoton resonance.** a) Transverse magnetization versus 2D frequency sweep. One, two and three photon resonance lines can be seen. b) Example time domain fields for the B_1 pulses generating a two-photon resonance and c) the corresponding frequency-domain fields. The three curves overlap in (c).

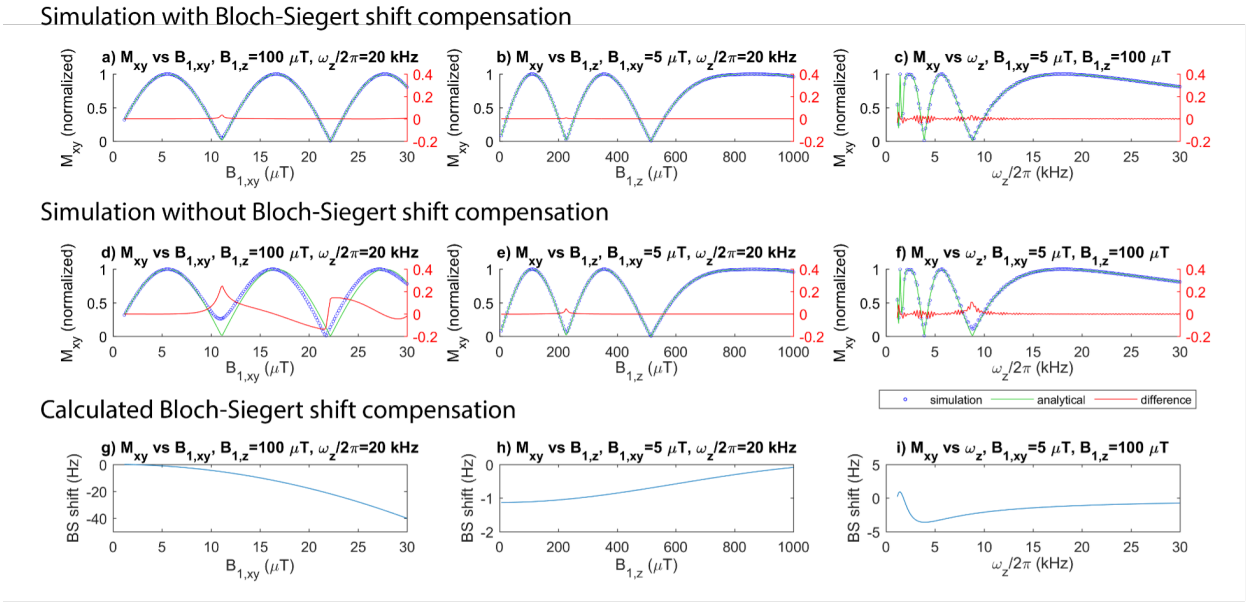

Figure 3.2: **BS-shifts for two-photon excitation for various parameters.** a-c) Simulation and analytical transverse magnetization for various $B_{1,xy}$, $B_{1,z}$, and ω_z respectively. In simulation, ω_{xy} values are set to be equal to ω_z with slight adjustments by the BS-shift as described in the text such that resonances are accurate. Differences between the simulated and analytical values are plotted in red with the axis on the right-hand side. d-f) Same as a-c, except that no BS-shift pre-adjustments are made for the simulations. Note that the differences between simulation and analytical transverse magnetization are nearly an order of magnitude more than in a-c for these ranges of parameters. g-i) BS-shifts calculated and used for the pre-adjustments in a-c simulations.

Chapter 4

Basic Scanner Experiments

This chapter presents verification of multiphoton resonances via basic MRI scanner experiments. To generate multiphoton excitation, two sources of z-direction RF were tested: an additional homebuilt coil and the built-in gradient coils in the MRI scanner. Because gradient coils are designed to produce z-direction magnetic fields, oscillating them produces z-direction RF.

4.1 Methods

All MRI experiments in this chapter except for the multiband RF pulses were performed on an Aspect 1T wrist scanner (Aspect Imaging, Shoham, Isreal). The multiband RF experiments were performed on a GE 3T MR750w scanner (Waukesha, WI, USA).

4.1.1 Experiment I: Two-Photon Excitation with an Extra z-RF Coil

Two-photon RF pulses were transmitted simultaneously with a commercial coil at 44.73 MHz (i.e. Larmor frequency plus 130 kHz) and a homebuilt solenoid coil at 130 kHz (Fig. 4.1) in the same manner as shown in Fig. 5 of [11]. The homebuilt coil, resonated and matched at 130 kHz, was inserted into the commercial coil, producing RF in the B_0 direction. The input to the 130-kHz coil was connected to a custom-built power amplifier (100 W, operational between 100 kHz to 1 MHz), which was connected to an arbitrary waveform generator (Keysight 33600A; gated burst mode and 130 kHz). The gating signal was synchronized to the scanner's control signal for the transmit/receive-switch, such that the 130 kHz signal was generated whenever the scanner transmitted a RF pulse. The 130 kHz shift was chosen as the shift is sufficiently large to avoid single-photon resonances. That is, all the frequencies transmitted by the two coils were outside of the range of single-photon excitation within the field of view. Gradient-echo images of a lemon were acquired with: TR/TE = 500/3.0 ms, FA = 10°, 500-µs sincgauss pulse, resolution = 0.625x0.625x3 mm^3, 80x80 mm^2 FOV,

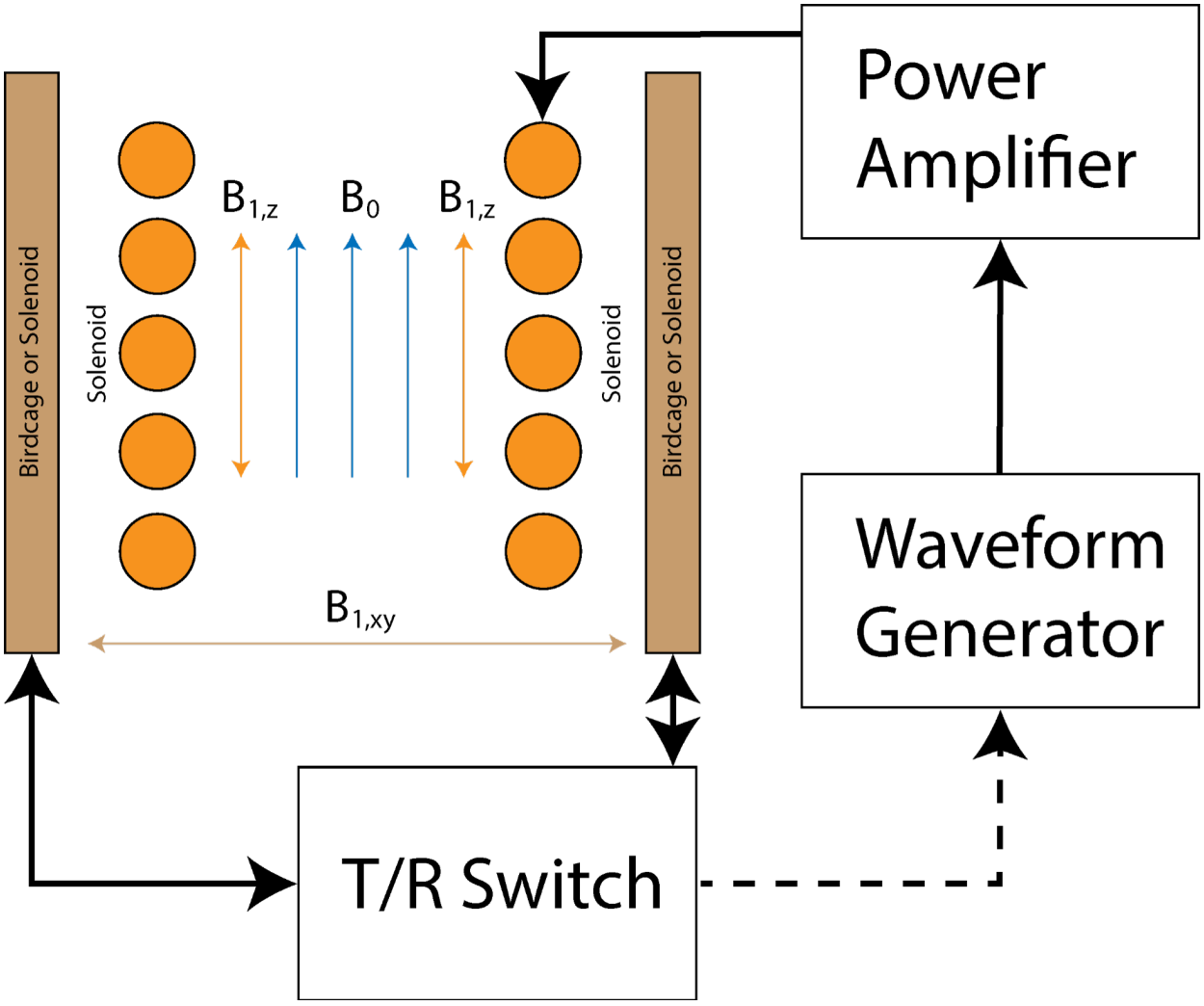

Figure 4.1: **Example two-photon scanning setup.** An extra $B_{1,z}$ solenoid is aligned with B_0. The control signal for the transmit/receive-switch (T/R switch) from the scanner triggers output from the waveform generator. The triggered 130 kHz signal is amplified and fed into the $B_{1,z}$ coil.

10 slices, 40-kHz readout bandwidth, axial orientation, 66-sec scan time. Gradient-echo images of a country-style pork rib were acquired with: TR/TE = 500/8.4 ms, FA = 45°, 10-ms sincgauss pulse, resolution = 0.625x0.625x2 mm^3, 80x80 mm^2 FOV, 10 slices, 40-kHz readout bandwidth, coronal orientation, 66-sec scan time.

4.1.2 Experiment 2: Two-Photon Excitation with Gradient Coils

Oscillating gradients can also provide z-axis RF. For example, given a sinusoidal gradient vector $\vec{\mathbf{G}}\sin(\omega_z t)$, the amplitude of the resulting z-axis RF is spatially linearly varying as

$$B_{1,z} = \vec{\mathbf{G}} \bullet \vec{\mathbf{r}}\ sin(\omega_z t) \tag{4.1}$$

The corresponding flip angles are thus also spatially varying following the nutation frequency in Eq. [2.16]. As an illustration, a copper-sulfate-solution phantom was non-selectively excited using the x or y gradient oscillating at 16 kHz in conjunction with an xy-RF offset by -16 kHz from the Larmor frequency. A Larmor-frequency 180° pulse was used to only refocus the center slice. Other parameters are: TR/TE = 500/8.4 ms, 700-µs excitation pulse (180° SLR RF pulse and 0.386 G/cm sinusoidal gradient), 700-µs 180° SLR refocusing pulse, resolution = 0.625x0.625x5 mm^3, 80x80 mm^2 FOV, 2 slices, 40-kHz readout bandwidth, axial orientation, 66-sec scan time.

4.1.3 Experiment 3: Multiband Multiphoton Adiabatic Pulse

Employing gradients for multiphoton excitation opens an avenue for novel pulse designs. As an example, we created a multiband multiphoton adiabatic inversion pulse by combining a standard hyperbolic secant adiabatic inversion pulse with an oscillating gradient, in contrast to previous approaches that add multiple pulses together [15] or periodically switch RF on and off [22]. As we have seen in Chapter 2, the multiphoton resonances look just like standard one-photon resonances in a particular rotating frame, so not only standard excitations, but also more exotic excitations such as adiabatic pulses generalize.

To implement it on the GE scanner, a fast spin echo pulse sequence with an inversion recovery module using a multiband hyperbolic secant inversion pulse was programmed in KSFoundation EPIC [33]. To view the multiband inversion profiles, the inversion-pulse gradients were applied along an axis perpendicular to the fast spin echo imaging plane. A plot of the pulse waveforms is shown in Fig. 4.2.

With a spherical phantom, we compared several combinations of RF and gradient waveforms with an inversion recovery time of 0.5 seconds. Firstly, we used an 8-ms hyperbolic secant RF pulse with parameters $A_0 = 22\ \mu T$, $\mu = 4.9$, and $\beta = 800$ rad/s. Adding a constant slice-selective 0.2 G/cm DC gradient results in a single inversion band. Superimposing a 3-kHz AC gradient with an amplitude equal to 1.5 times that of the DC gradient produces multiband inversion. This combination ensures that at the spatial locations where the local Larmor frequency is offset by 3 kHz from the center, $\frac{\gamma B_{1,z}}{\omega_z} = 1.5$, and the two-photon resonance is the most efficient resonance compared to any other resonance (Table 2.1). Similarly, at spatial locations with local Larmor frequencies offset by 6 kHz, we have $\frac{\gamma B_{1,z}}{\omega_z} = 3.0$ and the three-photon resonance is the most efficient resonance. Thus, for a field of view encompassing 6-kHz offsets in either direction, we expect a five-band adiabatic pulse composed of single-, two-, and three-photon adiabatic inversions (Fig. 4.3. Next, a 12-ms RF pulse ($\mu = 4$, and $\beta = 600$ rad/s) and a 0.2 G/cm DC gradient superimposed with a

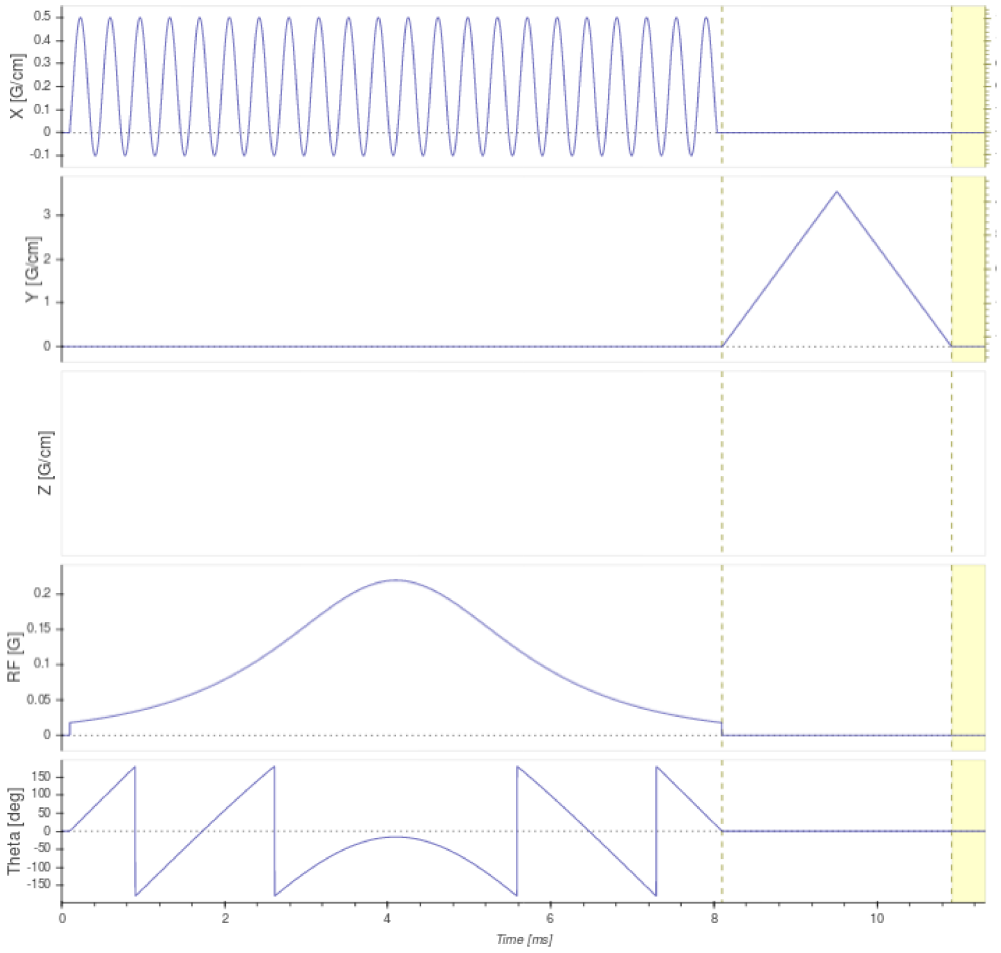

Figure 4.2: **Example multiband adiabatic pulse waveforms.** Waveform plot for multiphoton multiband adiabatic inversion pulse generated by KSFoundation Epic's sequence plotting. In this case, The DC gradient is 0.2 G/cm, the AC gradient is 1.5 times the DC gradient strength, and the hyperbolic secant RF pulse has nominal parameters $A_0 = 22\ \mu T$, $\mu = 4.9$, and $\beta = 800$ rad/s. The pulse duration is 8 ms. The AC gradient frequency is 2737.5 Hz, which leads to a maximum gradient slew rate of 51.6 T/m/s, which is well within standard hardware capabilities.

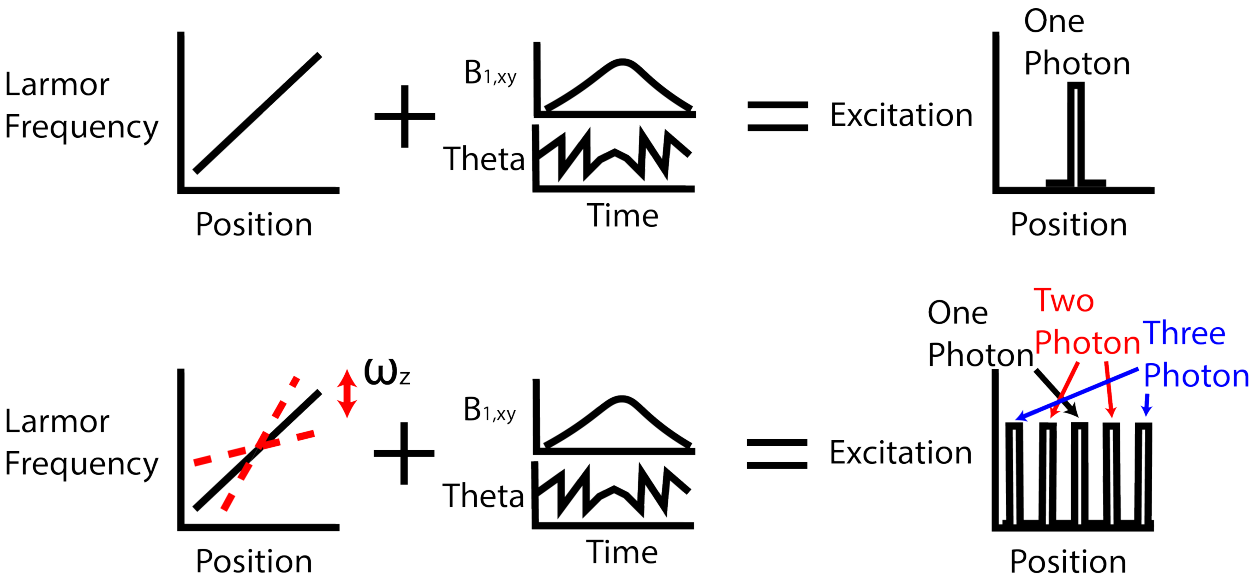

Figure 4.3: **Adiabatic multislice pulse concept.** Normally, an adiabatic RF pulse produces a single excitation band when combined with a slice selective gradient. However, when an AC gradient is superimposed on top of the slice select gradient, the one-photon band is unchanged and more bands are formed when multiphoton resonance conditions are met. This occurs when the local Larmor frequency offset is equal to an integer multiple of ω_z. If standard RF pulses were used instead of adiabatic pulses, the amount of excitation in each band would differ based on the relevant Bessel function scaling factor.

5.5-kHz AC gradient were used to produce three thinner bands. Finally, to demonstrate unevenly-spaced bands, the 12-ms pulse was applied with a 0.175 G/cm DC gradient that was superimposed with a 5.5-kHz and a 4-kHz AC gradient with amplitudes of 0.2625 and 0.175 G/cm respectively. These values were chosen such that higher-order bands were not formed in the field of view due to negligible excitation efficiency.

Under procedures approved by our institution's IRB, a healthy volunteer was scanned. For the human brain, the five bands produced by 8-ms multiphoton adiabatic inversion pulses as in the first phantom experiment were imaged with inversion recovery times of 400 ms, 650 ms, and 2500 ms. The parameters of the fast spin echo readout were: ETL = 8, TR/TE = 4000/44 ms, FA = 90°, FOV = 230x230 mm^2, matrix = 256x256, 1 slice of 2-mm thickness, 62.5-kHz readout bandwidth, axial orientation, 128-sec scan time.

4.2 Results

4.2.1 Experiment I: Two-Photon Excitation with an Extra z-RF Coil

With a spoiled gradient-echo sequence, the two-photon resonance produces similar image quality as those of the single-photon resonance for both the lemon and pork rib (Fig. 4.4). Spatial shading (Fig. 4.4b) is due to inhomogeneity of the $B_{1,z}$ coil and magnetic field deviations from the z-axis. SNR differences (Fig. 4.4c&d) are due to different tunings of the receive-coil frequency and thus matching with the low noise amplifier, as frequencies were tuned to $B_{1,xy}$ transmit frequencies on the transceiver coil. Any other slight SNR differences may be due to inaccurate flip angle calibration. As such, no quantitative SNR comparison is made.

4.2.2 Experiment 2: Two-Photon Excitation with Gradient Coils

When using gradients as a z-axis RF source, the frequency range is limited by the gradient slew rate, and the resulting RF field varies linearly in space (Eq. [4.1]). Different excitation patterns corresponding to different flip angles were generated with G_x and G_y gradient (Fig. 4.5a-d). When the z-axis RF (i.e. oscillating G_x and G_y) is turned off, no excitation occurs (Fig. 4.5e), demonstrating its two-photon nature. This two-photon excitation differs from spatial and spectral selective excitation that assumes RF transmitted and received both at the Larmor frequency and makes a small-tip approximation [29].

4.2.3 Experiment 3: Multiband Multiphoton Adiabatic Pulse

Fig. 4.6 shows the expected adiabatic inversion bands on a spherical phantom and human brain. It is possible to create more bands. However, as the Bessel function values become more dispersed with higher-order resonances, power efficiency for the higher-order multiphoton adiabatic inversions decrease and the total RF power needs to be increased to achieve full inversions for the higher-order resonances. Other frequencies in the rotating frame of the multiphoton resonance may also gain relative power and affect the success of the adiabatic pulse. Nevertheless, when producing multiple inversion bands, multiphoton resonances increase RF efficiency compared to the traditional method of adding independent pulses [15], as the same RF pulse produces excitation in each band. In theory, to achieve at least the same effective pulse amplitude for the multiband resonances as that of an original single-band pulse for single-photon resonance, we would need to multiply the RF amplitude by the inverse of the minimum Bessel function multiplier. In the five-band case with up to three-photon resonances shown, this is $1/J_2(3.0) = 2.06$. By multiplying RF amplitude by 2.06, we can achieve four extra bands, and if more ripple is acceptable in some bands, RF amplitude potentially need not even be increased at all. In comparison to [22], this method may be slightly less power efficient due to the less than or equal to unity Bessel function

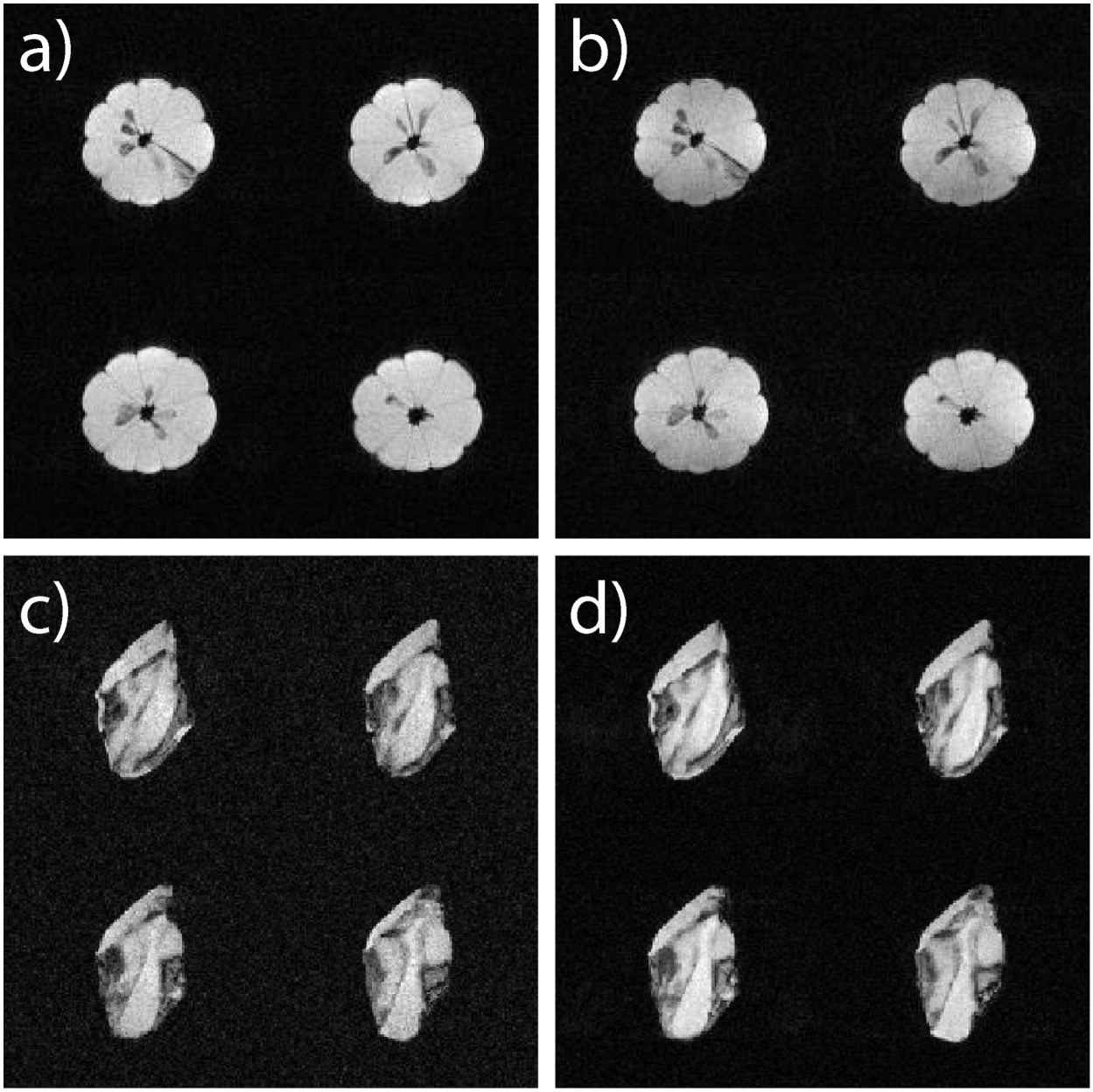

Figure 4.4: **Two-photon gradient-echo sequence.** a) Single-photon excitation for a lemon. b) Two-photon excitation for the lemon. c) Single-photon excitation for a country-style pork rib. d) Two-photon excitation for the pork rib. In (b) and (d), all transmit xy-RF was shifted up by 130 kHz and a 130-kHz square wave z-RF was transmitted simultaneously with the xy-RF.

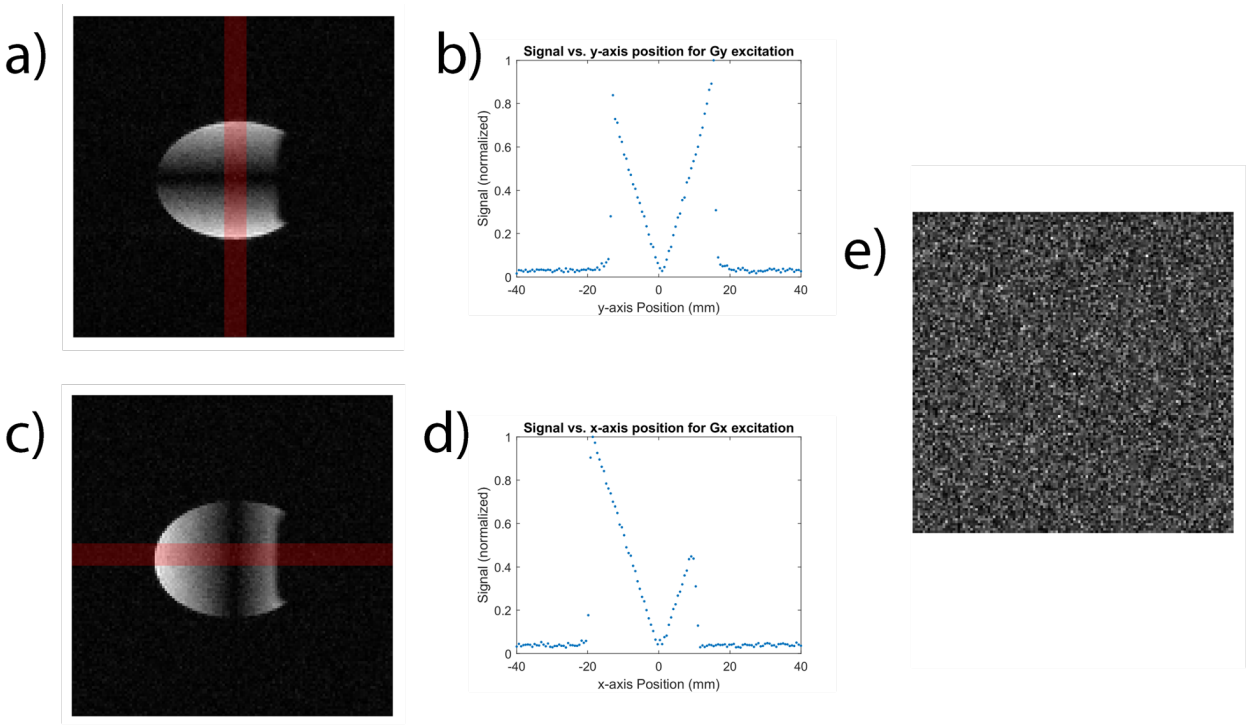

Figure 4.5: **Spin-echo with two-photon excitation.** a) Image acquired after excitation with RF offset by 16 kHz and G_y gradient (up/down direction) oscillating at 16 kHz and b) 1D line plot of signal vs. y-axis position for a center band of the image showing linear intensity variations as predicted by theory for small $\frac{\gamma B_{1,z}}{\omega_z}$ and flip angle. c) Excitation with RF offset by 16 kHz and G_x gradient (left/right direction) oscillating at 16 kHz and d) 1D line plot of signal vs. x-axis position for a center band of the image showing linear intensity variations. The red bands in (a) and (c) indicate the signal locations of (b) and (d) respectively. e) Excitation with RF offset by 16 kHz and no gradients.

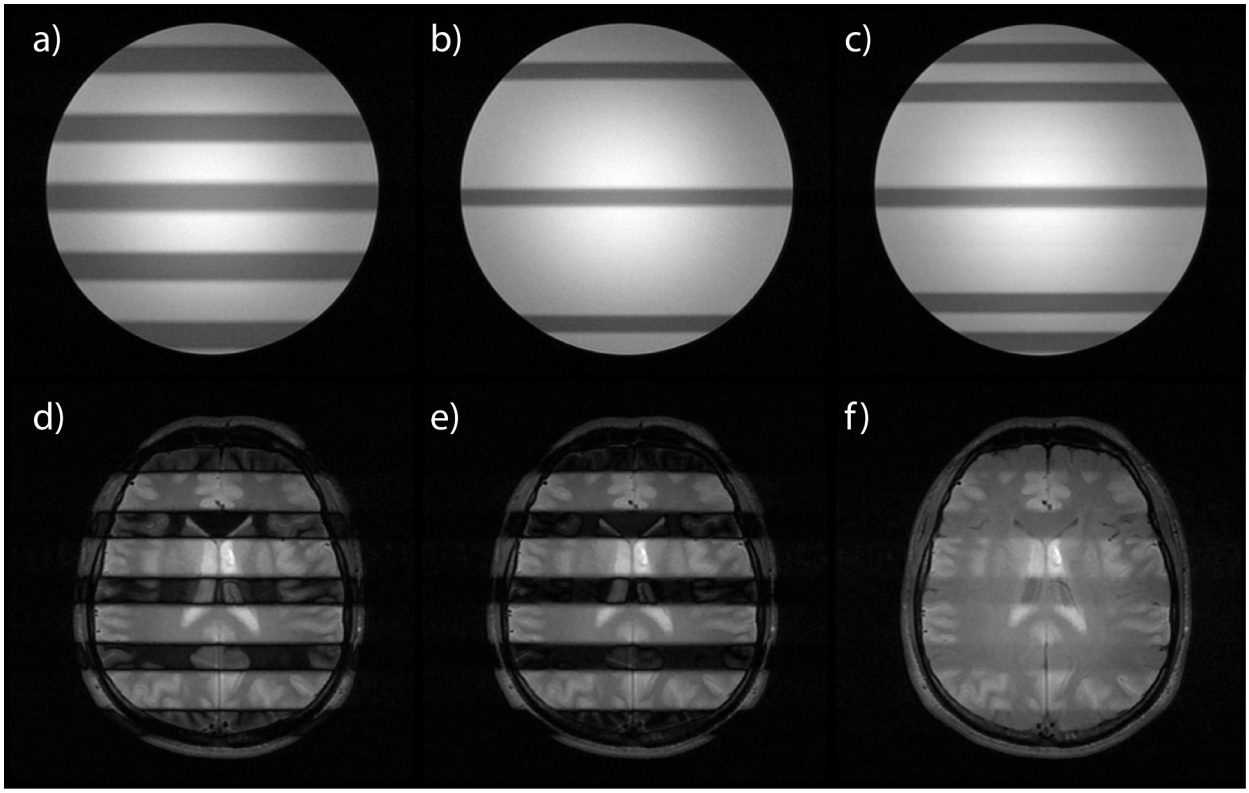

Figure 4.6: **Multiband adiabatic inversions on a spherical phantom and a human brain with various parameters.** a) An 8-ms hyperbolic secant RF pulse ($A_0 = 22\ \mu T$, $\mu = 4.9$, and $\beta = 800$ rad/s) with a 0.2 G/cm DC gradient and a 0.3 G/cm 3-kHz AC gradient. b) A 12-ms RF pulse ($\mu = 4$, and $\beta = 600$ rad/s) with a 0.2 G/cm DC gradient and a 0.3 G/cm 5.5-kHz AC gradient. c) The same RF as in (b) with a 0.175 G/cm DC gradient superimposed with a 5.5-kHz and a 4-kHz AC gradient with amplitudes of 0.2625 G/cm and 0.175 G/cm respectively. For the human brain, five-band multiphoton adiabatic inversion pulses as in (a) were imaged with inversion recovery times of d) 400 ms, e) 650 ms, and f) 2500 ms. The white matter, gray matter and CSF are seen to be selectively attenuated based on the inversion recovery time respectively.

factor, but it allows for much shorter pulses as the RF is not paused for gradients. Furthermore, the ability to make unevenly spaced pulses is potentially useful. 1D simulations of the inversion profiles for similar pulses are shown in Fig. 4.7.

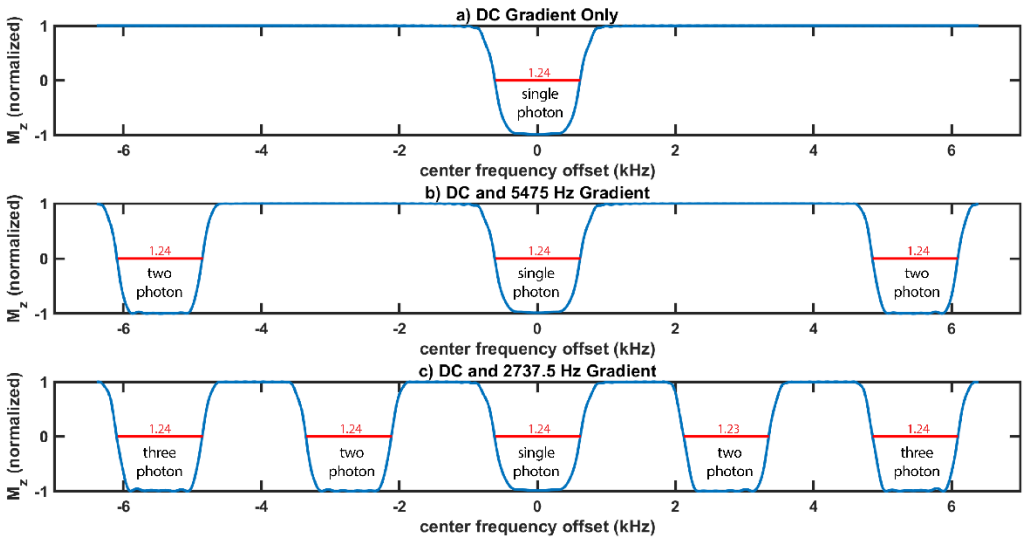

Figure 4.7: **Example multiband adiabatic pulse simulations.** An 8 ms hyperbolic secant RF pulse with parameters $A_0 = 22\ \mu T$, $\mu = 4.9$, and $\beta = 800$ rad/s is simulated with a) only a DC gradient, b) a DC gradient and a 5475 Hz gradient with 1.5 times the amplitude of the DC, and c) a DC gradient and a 2737.5 Hz gradient with 1.5 times the amplitude of the DC. One, three, and five adiabatic inversion bands can respectively be seen in the field of view. Red numbers indicate the full width half maximum (FWHM) in kHz. Any slight differences in FWHM may be due to slight asymmetries in the BS-shift or numerical error.

Chapter 5

Multiphoton Selective Excitation Theory

The previous chapters attempted to provide intuition for multiphoton excitation by giving analogies to one-photon excitation via the phase-modulated rotating frame. This chapter describes the general principles of multiphoton pulsed selective excitation, providing a formalized treatment. We treat the spatial and temporal dynamics of multiphoton excitation using the Bloch equations for the purpose of designing general excitation pulses with single or multiple RF coils. In the following derivations, we will make use of several terms which are defined in Section 10.1. Note that based on the geometrical representation of the Schrödinger equation, the Bloch equations of vector rotations are equivalent to the quantum mechanical description in an ideal spin $\frac{1}{2}$ system or any other ideal quantum mechanical two-level system [14].

5.1 Bloch Equations for Multiphoton Excitation

The Bloch equations can be written as

$$\begin{bmatrix} \dot{M}_x \\ \dot{M}_y \\ \dot{M}_z \end{bmatrix} = \gamma \begin{bmatrix} 0 & B_z(t) & -B_y(t) \\ -B_z(t) & 0 & B_x(t) \\ B_y(t) & -B_x(t) & 0 \end{bmatrix} \begin{bmatrix} M_x \\ M_y \\ M_z \end{bmatrix} + \begin{bmatrix} -\frac{M_x}{T_2} \\ -\frac{M_y}{T_2} \\ -\frac{M_z - M_0}{T_1} \end{bmatrix}. \tag{5.1}$$

With a small-tip angle approximation and ignoring relaxation, we can approximate $M_z(t) \approx M_0$. As a result, Eq. 5.1 becomes

$$\begin{bmatrix} \dot{M}_x \\ \dot{M}_y \end{bmatrix} = \gamma \begin{bmatrix} 0 & B_z(t) \\ -B_z(t) & 0 \end{bmatrix} \begin{bmatrix} M_x \\ M_y \end{bmatrix} + \gamma \begin{bmatrix} -B_y(t)M_0 \\ B_x(t)M_0 \end{bmatrix}. \tag{5.2}$$

Denote the transverse magnetization and magnetic field as

$$m_{xy} = M_x + iM_y, \tag{5.3}$$

$$B_{xy} = B_x + iB_y. \tag{5.4}$$

For pulsed B fields over the time period from 0 to T, the solution to Eq. [5.2] which describes the transverse magnetization resulting from excitation, is given by

$$m_{xy}(\mathbf{r}, T) = i\gamma\ M_0 \int_0^T B_{xy}(\mathbf{r}, t) e^{-i\gamma \int_t^T B_z(\mathbf{r},\tau)d\tau} dt. \tag{5.5}$$

The spatial and temporal profiles of the B fields provide the flexibility to design RF pulses that can optimize the excitation profiles. For simplicity, we assume that the RF coils generate spatially uniform fields with the addition of a linear gradient field. In addition to the standard RF coil in the xy-direction providing $B_{1,xy}$ fields, we also assume a RF coil in the z-direction providing $B_{1,z}$ fields. For additional flexibility, we also assume that the RF coil in the z-direction can provide near-DC uniform magnetic fields $B_{DC,z}$. With these fields, in the Larmor frequency rotating frame,

$$B_z = B_{1,z}(t)\cos(\omega_z t + \phi(t)) + B_{DC,z}(t) + \mathbf{G}(t) \bullet \mathbf{r}, \tag{5.6}$$

$$B_x = B_{1,xy}(t)\cos((\omega_{xy} - \omega_0)t + \theta(t)), \tag{5.7}$$

$$B_y = -B_{1,xy}(t)\sin((\omega_{xy} - \omega_0)t + \theta(t)), \tag{5.8}$$

$$B_{xy} = B_{1,xy}(t) e^{-i((\omega_{xy}-\omega_0)t+\theta(t))}. \tag{5.9}$$

Under these conditions, Eq. [5.5]

$$m_{xy}(\mathbf{r}, T) = i\gamma\ M_0 \int_0^T B_{1,xy}(t) e^{-i((\omega_{xy}-\omega_0)t+\theta(t))} e^{-i\gamma \int_t^T B_{1,z}(\tau)\cos(\omega_z\tau+\phi(\tau))d\tau} e^{-i\gamma \int_t^T B_{DC,z}(\tau)d\tau} e^{-i\gamma \int_t^T \mathbf{G}(\tau)\bullet\mathbf{r}d\tau} dt. \tag{5.10}$$

Under the condition of multiphoton excitation, $\omega_{xy} - \omega_0 = n\omega_z$, Eq. [5.10] can be rewritten as

$$m_{xy}(\mathbf{r}, T) = i\gamma\ M_0 \int_0^T B_{1,xy}(t) e^{-i(n\omega_z t+\theta(t))} e^{-i\gamma \int_t^T B_{1,z}(\tau)\cos(\omega_z\tau+\phi(\tau))d\tau} e^{-i\gamma \int_t^T B_{DC,z}(\tau)d\tau} e^{i\mathbf{k}(t)\bullet\mathbf{r}} dt, \tag{5.11}$$

where $-\gamma \int_t^T \mathbf{G}(\tau)d\tau = \mathbf{k}(t)$ as in excitation k-space [36]. Eq. [5.11] shows that the contribution of a spatially uniform B_z pulse $e^{-i\gamma \int_t^T B_{1,z}(\tau)\cos(\omega_z\tau+\phi(\tau))d\tau} e^{-i\gamma \int_t^T B_{DC,z}(\tau)d\tau}$ can be equivalent to a phase/frequency modulation of the B_{xy} pulse, represented by $\theta(t)$. However, if ω_z is relatively large, bandwidth constraints in the RF system may make phase modulation of the B_{xy} pulse less practical. Phase modulating the B_{xy} pulse to achieve excitation would also cause the B_{xy} pulse to have a frequency component at the Larmor frequency, as expected since it is still standard one-photon excitation, which is not the case in multiphoton excitation.

5.2 Multiphoton Selective Excitation Designs

5.2.1 Constant-$B_{1,z}$ Pulses

If $B_{1,z}$ and ϕ are time invariant, i.e. a hard pulse, and assuming that $\omega_z \neq 0$, the integral involving $B_{1,z}(t)$ in Eq. [5.11] can be evaluated analytically as follows,

$$m_{xy}(\mathbf{r},T) = i\gamma M_0 \int_0^T B_{1,xy}(t) e^{-i(n\omega_z t+\theta(t))} e^{-i\frac{\gamma B_{1,z}}{\omega_z}(\sin(\omega_z T+\phi)-\sin(\omega_z t+\phi))} e^{-i\gamma B_{DC,z}(T-t)} e^{i\mathbf{k}(t)\bullet\mathbf{r}} dt \tag{5.12}$$

$$m_{xy}(\mathbf{r},T) = i\gamma\ M_0 e^{-i\frac{\gamma B_{1,z}}{\omega_z}\sin(\omega_z T+\phi)} e^{-i\gamma B_{DC,z}T} \int_0^T B_{1,xy}(t) e^{-i(n\omega_z t+\theta(t))} e^{i\frac{\gamma B_{1,z}}{\omega_z}\sin(\omega_z t+\phi)} e^{i\gamma B_{DC,z}t} e^{i\mathbf{k}(t)\bullet\mathbf{r}} dt. \tag{5.13}$$

Using the Jacobi-Anger expansion shown below, where $J_m(-)$ is the Bessel function of the first kind of order m,

$$e^{i\frac{\gamma B_{1,z}}{\omega_z}\sin(\omega_z t+\phi)} = \sum_{m=-\infty}^{\infty} J_m(\frac{\gamma B_{1,z}}{\omega_z}) e^{im(\omega_z t+\phi)}, \tag{5.14}$$

Eq. [5.13] can be rewritten as

$$m_{xy}(\mathbf{r},T) = i\gamma\ M_0 e^{-i\frac{\gamma B_{1,z}}{\omega_z}\sin(\omega_z T+\phi)} e^{-i\gamma B_{DC,z}T} \int_0^T B_{1,xy}(t) e^{-i(n\omega_z t+\theta(t))} \left(\sum_{m=-\infty}^{\infty} J_m(\frac{\gamma B_{1,z}}{\omega_z}) e^{im(\omega_z t+\phi)}\right) e^{i\gamma B_{DC,z}t} e^{i\mathbf{k}(t)\bullet\mathbf{r}} dt. \tag{5.15}$$

For a given n, i.e. n z-photon excitation, the integral in Eq. [5.15] is only significant for the term involving m = n in that the fast oscillating terms mostly average out. If we assume that the bandwidths of time-varying terms are small relative to ω_z, Eq. [5.15] can be simplified as

$$m_{xy}(\mathbf{r},T) = i\gamma\ M_0 e^{-i(\frac{\gamma B_{1,z}}{\omega_z}\sin(\omega_z T+\phi)-n\phi)} e^{-i\gamma B_{DC,z}T} J_n(\frac{\gamma B_{1,z}}{\omega_z}) \int_0^T B_{1,xy}(t) e^{-i\theta(t)} e^{i\gamma B_{DC,z}t} e^{i\mathbf{k}(t)\bullet\mathbf{r}} dt. \tag{5.16}$$

Eq. [5.16] shows that, if B_z is a hard pulse, it only adds a constant phase shift and amplitude scaling to the excitation. The slice profile and selection are determined entirely by B_{xy}. Like in the one-photon case, the slice location can be chosen by setting $\theta(t) = \Delta\omega t$, where $\Delta\omega$ is some frequency offset. While not commonly implemented in modern MRI but used historically, setting $B_{DC,z}$ to a non-zero value can also shift the slice.

Interestingly, in the multiphoton case, slice selection can also be achieved by shifting the frequency of B_z instead. Specifically, replacing ω_z with a new frequency of $\omega_z + \Delta\omega$ and assuming $B_{DC,z} = 0$, Eq. [5.10] becomes

$$m_{xy}(\mathbf{r},T) = i\gamma M_0 \int_0^T B_{1,xy}(t) e^{-i((\omega_{xy}-\omega 0)t+\theta(t))} e^{-i\gamma\int_t^T B_{1,z}(\tau)\cos((\omega_z+\Delta\omega)\tau+\phi)d\tau} e^{-i\gamma\int_t^T \mathbf{G}(\tau)\bullet\mathbf{r}d\tau} dt \tag{5.17}$$

Then, following the same steps to Eq. [5.16] while keeping $\omega_{xy} - \omega_0 = n\omega_z$ so that the frequency of B_{xy} stays the same, we get

$$m_{xy}(\mathbf{r},T) = i\gamma M_0 e^{-i(\frac{\gamma B_{1,z}}{\omega_z}\sin((\omega_z+\Delta\omega)T+\phi)-n\phi)} J_n\left(\frac{\gamma B_{1,z}}{\omega_z+\Delta\omega}\right) \int_0^T B_{1,xy} e^{-i\theta(t)} e^{in\Delta\omega t} e^{i\mathbf{k}(t)\bullet\mathbf{r}} dt \tag{5.18}$$

The slice excitation location is determined by the frequency shift of $\Delta\omega$, the order of the multiphoton excitation, and the amplitude of the gradients. The effect is similar to choosing a different frequency for B_{xy} via $\theta(t)$.

We see that when we have access to a uniform B_z field, we are given three options for positioning a slice with multiphoton excitation: shifting the frequency of B_{xy}, adding a DC B_z, or shifting the frequency of B_z.

5.2.2 Shaped-B_z Pulses

If $B_{1,z}(\tau)$ is slowly varying compared to $\cos(\omega_{1,z}\tau)$ and $\phi(\tau)$ is slowly varying compared to $\omega_{1,z}\tau$, then we can make some approximations that give us more design intuition than Eq. [5.11] in the general non-hard pulse case. We will make these assumptions more precise later. With the trigonometric identity

$$\cos(\omega_z\tau + \phi(\tau)) = \cos(\omega_z\tau)\cos(\phi(\tau)) - \sin(\omega_z\tau)\cos(\phi(\tau)), \tag{5.19}$$

we can rewrite Eq. [5.11] as

$$m_{xy}(\mathbf{r},T) = i\gamma\, M_0 \int_0^T B_{1,xy}(t)\, e^{-i(n\omega_z t+\theta(t))} e^{-i\gamma\int_t^T B_{1,z}(\tau)(\cos(\omega_z\tau)\cos(\phi(\tau))-\sin(\omega_z\tau)\sin(\phi(\tau)))d\tau} e^{-i\gamma\int_t^T B_{DC,z}(\tau)d\tau} e^{i\mathbf{k}(t)\bullet\mathbf{r}} dt, \tag{5.20}$$

Using integration by parts,

$$\int_t^T B_{1,z}(\tau)\cos(\omega_z\tau)\cos(\phi(\tau))d\tau = \left[B_{1,z}(\tau)\cos(\phi(\tau))\frac{\sin(\omega_z\tau)}{\omega_z}\right]_t^T - \int_t^T \frac{\sin(\omega_z\tau)}{\omega_z}\frac{d}{d\tau}\left[B_{1,z}(\tau)\cos(\phi(\tau))\right]d\tau \tag{5.21}$$

and

$$\int_t^T B_{1,z}(\tau)\sin(\omega_z\tau)\sin(\phi(\tau))d\tau = \left[B_{1,z}(\tau)\sin(\phi(\tau))\frac{-\cos(\omega_z\tau)}{\omega_z}\right]_t^T - \int_t^T \frac{-\cos(\omega_z\tau)}{\omega_z}\frac{d}{d\tau}\left[B_{1,z}(\tau)\sin(\phi(\tau))\right]d\tau \quad (5.22)$$

If the terms $\int_t^T \frac{\sin(\omega_z\tau)}{\omega_z}\frac{d}{d\tau}\left[B_{1,z}(\tau)\cos(\phi(\tau))\right]d\tau$ and $\int_t^T \frac{-\cos(\omega_z\tau)}{\omega_z}\frac{d}{d\tau}\left[B_{1,z}(\tau)\sin(\phi(\tau))\right]d\tau$ are negligible, then

$$\begin{aligned}\int_t^T B_{1,z}(\tau)(\cos(\omega_z\tau)\cos(\phi(\tau)) - \sin(\omega_z\tau)\sin(\phi(\tau)))d\tau \\ \approx \left[B_{1,z}(\tau)\cos(\phi(\tau))\frac{\sin(\omega_z\tau)}{\omega_z}\right]_t^T - \left[B_{1,z}(\tau)\sin(\phi(\tau))\frac{-\cos(\omega_z\tau)}{\omega_z}\right]_t^T \\ = \frac{1}{\omega_z}\left(B_{1,z}(T)\sin(\omega_z T+\phi(T)) - B_{1,z}(t)\sin(\omega_z t+\phi(t))\right) \quad (5.23)\end{aligned}$$

by the angle addition identity. Plugging this back in, Eq. [5.20] becomes

$$m_{xy}(\mathbf{r},T) \approx i\gamma M_0\int_0^T B_{1,xy}(t)\,e^{-i(n\omega_z t+\theta(t))}e^{-i\frac{\gamma}{\omega_z}(B_{1,z}(T)\sin(\omega_z T+\phi(T))-B_{1,z}(t)\sin(\omega_z t+\phi(t)))} e^{-i\gamma\int_t^T B_{DC,z}(\tau)d\tau}e^{i\mathbf{k}(t)\bullet\mathbf{r}}dt \quad (5.24)$$

Applying Eq. [15.14 like before,

$$m_{xy}(\mathbf{r},T) \approx i\gamma M_0\int_0^T B_{1,xy}(t)\,e^{-i(n\omega_z t+\theta(t))}\left(\sum_{m=-\infty}^{\infty} J_m\left(\frac{\gamma B_{1,z}(t)}{\omega_z}\right)e^{im(\omega_z t+\phi(t))}\right) e^{-i\frac{\gamma B_{1,z}(T)}{\omega_z}\sin(\omega_z T+\phi(T))}e^{-i\gamma\int_t^T B_{DC,z}(\tau)d\tau}e^{i\mathbf{k}(t)\bullet\mathbf{r}}dt \quad (5.25)$$

This is just like Eq. [5.15], except that $J_m\left(\frac{\gamma B_{1,z}(t)}{\omega_z}\right)e^{im\phi(t)}$ and $B_{DC,z}(\tau)$ are also time-varying. If the bandwidth of $J_m\left(\frac{\gamma B_{1,z}(t)}{\omega_z}\right)e^{im\phi(t)}$ and the other time varying terms are small relative to $(m-n)\omega_z$, then like with Eq. [5.15], only the term with m = n contributes significantly to the integral. The fast oscillating off-resonant terms essentially average out in the integral, whereas the resonant term with $m = n$ is much more important. This results in

$$m_{xy}(\mathbf{r},T) \approx i\gamma M_0\int_0^T B_{1,xy}(t)e^{-i\theta(t)}J_n\left(\frac{\gamma B_{1,z}(t)}{\omega_z}\right) e^{-i(\frac{\gamma B_{1,z}(T)}{\omega_z}\sin(\omega_z T+\phi(T))-n\phi(t))}e^{-i\gamma\int_t^T B_{DC,z}(\tau)d\tau}e^{i\mathbf{k}(t)\bullet\mathbf{r}}dt \quad (5.26)$$

Eq. [5.26] shows that B_{xy} and B_z contribute to the excitation profile in a similar way with $B_{1,xy}(t)$ corresponding to $J_n\left(\frac{\gamma B_{1,z}(t)}{\omega_z}\right)$ and $e^{-i\theta(t)}$ corresponding to $e^{-i(\frac{\gamma B_{1,z}(T)}{\omega_z}\sin(\omega_z T+\phi(T))-n\phi(t))}e^{-i\gamma\int_t^T B_{DC,z}(\tau)d\tau}$, which represent amplitude and phase modulation respectively. So, amplitude and phase modulation can be done with B_{xy} or B_z independently, or with a combination of the two. Amplitude modulation via $B_{1,z}$ appears more complicated due to the Bessel function, but this is due to the asymmetry of the setup. In the two-photon case where n, the number of z-photons involved, is one, J_1 is approximately linear for small values of $\frac{\gamma B_{1,z}(t)}{\omega_z}$. So, when our z-RF is like the standard xy-RF where the RF amplitude is very small compared to the frequency, the effective z-RF amplitude modulation is simply directly proportional to the actual amplitude modulation. However, for excitation efficiency, we often want to operate in the regime where $\gamma B_{1,z}(t)$ becomes comparable to ω_z and beyond. In this regime, J_1 takes the form of a dampened, aperiodic sine wave with a maximum value of about 0.58 at $\frac{\gamma B_{1,z}(t)}{\omega_z} = 1.84$. For higher order excitations with n¿1, for small values of $\frac{\gamma B_{1,z}(t)}{\omega_z}$ the Bessel functions are quadratic for n=2, cubic for n=3, etc. For larger values of $\frac{\gamma B_{1,z}(t)}{\omega_z}$, the higher order Bessel functions also become dampened, aperiodic sinusoids.

For phase modulation, the z-RF is very similar to the xy-RF, except that there is an extra constant term, and the phase modulation is multiplied by the number of z-photons involved, n. When n=1 in the two-photon case, then z-RF phase modulation acts just like xy-RF phase modulation. When more z-photons are simultaneously involved, somewhat intuitively, they each contribute to the phase. When there is an additional coil producing z-direction magnetic fields, not only can the RF vary the phase, but the additional $B_{DC,z}$ term can also vary the phase.

5.2.3 Assumptions for Shaped-$B_{1,z}$ Pulse Analysis

Let us discuss a little about the assumptions from the previous section. They are listed in the following.

1. $\int_t^T \frac{\sin(\omega_z\tau)}{\omega_z}\frac{d}{d\tau}\left[B_{1,z}(\tau)\cos(\phi(\tau))\right]d\tau$ is negligible compared to $\left[B_{1,z}(\tau)\cos(\phi(\tau))\frac{\sin(\omega_z\tau)}{\omega_z}\right]_t^T$.
2. $\int_t^T \frac{-\cos(\omega_z\tau)}{\omega_z}\frac{d}{d\tau}\left[B_{1,z}(\tau)\sin(\phi(\tau))\right]d\tau$ is negligible compared to $\left[B_{1,z}(\tau)\sin(\phi(\tau))\frac{-\cos(\omega_z\tau)}{\omega_z}\right]_t^T$.
3. The bandwidth of $J_m\left(\frac{\gamma B_{1,z}(t)}{\omega_z}\right)e^{im\phi(t)}$ is small relative to $(m-n)\omega_z$.

For more intuition on assumption 1, since it is a bit difficult to compare an integral with a value, we can apply integration by parts again to obtain

$$\begin{aligned}&\int_t^T \frac{\sin(\omega_z\tau)}{\omega_z}\frac{d}{d\tau}\left[B_{1,z}(\tau)\cos(\phi(\tau))\right]d\tau \\ &= \left[\frac{d}{d\tau}\left[B_{1,z}(\tau)\cos(\phi(\tau))\right]\frac{-\cos(\omega_z\tau)}{{\omega_z}^2}\right]_t^T - \int_t^T \frac{-\cos(\omega_z\tau)}{{\omega_z}^2}\frac{d^2}{d\tau^2}\left[B_{1,z}(\tau)\sin(\phi(\tau))\right]d\tau\end{aligned} \tag{5.27}$$

For the first term on the right hand side of Eq. [5.27] to be negligible, we want $\frac{\frac{d}{d\tau}[B_{1,z}(\tau)\cos(\phi(\tau))]}{{\omega_z}^2} \ll \frac{B_{1,z}(\tau)\cos(\phi(\tau))}{\omega_z}$ or $\frac{\frac{d}{d\tau}[B_{1,z}(\tau)\cos(\phi(\tau))]}{\omega_z} \ll B_{1,z}(\tau)\cos(\phi(\tau))$ for all time. This assumption becomes more reasonable as ω_z increases. For the second term, we can continue to expand it with integration by parts infinitely, obtaining more terms with higher and higher order derivatives. In the same spirit as the slowly varying amplitude approximation [6] often used in optics though, we can often directly consider these higher order derivatives to be negligible. Assumption 2 follows the same logic.

In order for assumption 3 to be true, $B_{1,z}(t)$ and $\phi(t)$ must be slowly varying such that the Fourier transforms of their relevant terms have negligible frequency components near $(m-n)\omega_z$, so that $e^{-in\omega_z t}J_m\left(\frac{\gamma B_{1,z}(t)}{\omega_z}\right)e^{im(\omega_z t+\phi(t))}$ only consists of fast oscillating components when m is not equal to n. Since J_m is a nonlinear function, generally, harmonics of $\frac{\gamma B_{1,z}(t)}{\omega_z}$ are produced and for the assumption to be true, these should also have negligible frequency components near $(m-n)\omega_z$. As long as the variation in $\frac{\gamma B_{1,z}(t)}{\omega_z}$ is relatively small though, the power in the harmonics generated by $J_m\left(\frac{\gamma B_{1,z}(t)}{\omega_z}\right)$ is also likely small. To make this assumption more easily satisfied, $J_m\left(\frac{\gamma B_{1,z}(t)}{\omega_z}\right)$ instead of $B_{1,z}(t)$ can be directly designed just like $B_{1,xy}(t)$. Then, with a target $J_m\left(\frac{\gamma B_{1,z}(t)}{\omega_z}\right)$, $B_{1,z}(t)$ can be solved for.

Note that unlike Eq. [5.18], the frequency/phase modulation of the B_z pulse in Eq. [5.26] does not appear inside the Bessel function. This is because in Eq. [5.26], the equivalent of $\omega_z \gg \Delta\omega$ is assumed.

5.2.4 Constant-$B_{1,xy}$ Pulses

If B_{xy} is chosen as a hard pulse, Eq. [5.26] becomes

$$\begin{aligned}&m_{xy}(\mathbf{r},T) \\ &\approx i\gamma M_0 B_{1,xy}e^{-i\theta}\int_0^T J_n\left(\frac{\gamma B_{1,z}(t)}{\omega_z}\right)e^{-i\left(\frac{\gamma B_{1,z}(T)}{\omega_z}\sin(\omega_z T+\phi(T))-n\phi(t)+\gamma\int_t^T B_{DC,z}(t)d\tau\right)}e^{i\mathbf{k}(t)\bullet\mathbf{r}}dt\end{aligned} \tag{5.28}$$

We can observe correspondences between Eq. [5.28] and Eq. [5.16]. If B_{xy} is a hard pulse, it only adds a constant phase shift and amplitude scaling. The slice profile and selection are determined entirely by B_z. Slice position can still be changed with the same three options as described in the Constant-$B_{1,z}$ Pulses section.

5.2.5 Simultaneous Multislice Excitation

In conventional one-photon excitation, multiple slices can be excited simultaneously by modulating the B_{xy} field, e.g. by a trigonometric function. However, this approach increases the RF power and SAR deposition proportionally to the number of slices. With multiphoton excitation, we can shift the modulation to the B_z field. As the B_z field has orders of magnitude lower frequency, the resulting SAR increase is negligible. While a uniform B_z field or the corresponding frequency modulation of the B_{xy} field can distribute RF power to multiple frequencies, like the trigonometric modulation, neither have SAR benefits. Instead, a non-uniform B_z field can be used. Like before, we cabn use fast oscillating gradients as a source of spatially linearly varying z-direction RF. With this approach, a single-frequency B_{xy} field produced by a transmit coil can excite multiple spatial locations with different local Larmor frequencies using different multiphoton resonance conditions, thus reducing the need to increase transmit power. We previously used adiabatic pulses to compensate for the nonuniform excitation caused by spatially varying B_z field. Here we analyze the design of non-adiabatic multiphoton multislice pulses more generally, but with ϕ as a constant for simplicity. Rewrite Eq. [5.6] as

$$B_z = (\mathbf{G_{1,z}}(t) \bullet \mathbf{r} + B_{1,z}(t)) \cos(\omega_z t + \phi) + \mathbf{G}(t) \bullet \mathbf{r} \tag{5.29}$$

Now B_z consists of a uniform RF field as well as gradient fields, produced by the same physical coils, split between a near-DC component ($\mathbf{G}$) and an oscillating component with frequency of ω_z ($\mathbf{G_{1,z}}$). With Eq. [5.29], Eq. [5.10] becomes

$$m_{xy}(\mathbf{r}, T) = i\gamma M_0 \int_0^T B_{1,xy}(t) e^{-i((\omega_{xy}-\omega_0)t+\theta(t))} e^{-i\gamma \int_t^T (\mathbf{G_{1,z}}(t)\bullet\mathbf{r}+B_{1,z}(t)) \cos(\omega_z t+\phi) d\tau} e^{i\mathbf{k}(t)\bullet\mathbf{r}} dt. \tag{5.30}$$

If we design the RF pulses such that 1) $\omega_{xy} = \omega_0$, and 2) $\mathbf{G_{1,z}}(t) \bullet \mathbf{r} + B_{1,z}(t)$ varies much more slowly than $\cos(\omega_z t + \phi)$, then, by applying the Jacobi-Anger expansion as in previous sections, Eq. [5.30] becomes

$$m_{xy}(\mathbf{r}, T) \approx i\gamma M_0 \int_0^T \sum_{m=-\infty}^{\infty} J_m\left(\frac{\gamma(\mathbf{G_{1,z}}(t) \bullet \mathbf{r} + B_{1,z}(t))}{\omega_z}\right) B_{1,xy}(t) e^{im\omega_z t} e^{-i(\frac{\gamma(\mathbf{G_{1,z}}(T)\bullet\mathbf{r}+B_{1,z}(T))}{\omega_z} \sin(\omega_z T+\phi)-m\phi)} e^{-i\theta(t)} e^{i\mathbf{k}(t)\bullet\mathbf{r}} dt \tag{5.31}$$

Each discrete frequency ($m\omega_z$) permits the selective excitation of a slice. The amplitudes of these frequencies (J_m) are spatially dependent, which allows for reduced SAR, as described

before, while the uniform $B_{1,z}(t)$ term allows for more flexibility to control the spatial dependence. Without the uniform term, only one-photon excitation could have a contribution at the isocenter because for $\mathbf{r} = \mathbf{0}$ and $B_{1,z}(t) = 0$, we would have $\sum_{m=-\infty}^{\infty} J_m(0) B_{1,xy}(t) e^{im\omega_z t} e^{im\phi} = J_0(0) B_{1,xy}(t)$ as Bessel functions are zero at zero except for the 0th order. If a uniform $B_{1,z}$ field is not available, $\theta(t)$ can be utilized instead to perform the same function, as shown in the section Bloch Equations for Multiphoton Excitation.

Chapter 6

Multiphoton Selective Excitation Experiments

6.1 Methods

6.1.1 Overview of Pulse Design and Simulation

To demonstrate the principles described in the theory, we simulated and implemented four sets of related pulses, each set demonstrating a different principle. The first three sets utilized a uniform B_z field, while the last set demonstrated multislice excitation with oscillating gradients. Simulations based on Eq. [5.1] were written in Python and the code is available at https://github.com/LiuCLab/multiphoton-selective-excitation. To generate each pulse in the first three sets, the following procedure was followed.

1. Generate a prototype pulse together with gradients using a conventional method like the SLR algorithm [35].
2. If designing a standard one-photon pulse, directly set B_{xy} to the prototype pulse and finish.
3. Else if designing a multiphoton or corresponding frequency-modulated pulse, choose ω_z.
   a) Based on Eq. [5.26], choose values such that $B_{1,xy}(t)J_n\left(\frac{\gamma B_{1,z}(t)}{\omega_z}\right)$ equals the amplitude modulation of the prototype pulse, and $e^{-i\theta(t)}e^{-i(\frac{\gamma B_{1,z}(T)}{\omega_z}\sin(\omega_z T+\phi(T))-n\phi(t))}e^{-i\gamma\int_t^T B_{DC,z}(\tau)d\tau}$ equals the frequency modulation of the prototype pulse. A different equation instead of Eq. [5.26] may be used in specific situations, but the same principle of matching amplitude and frequency modulations applies. When either B_z or B_{xy} is chosen to be a hard pulse, they simply result in scaling factors.
   b) Shift the center frequency of the B_{xy} pulse by $n\omega_z$, assuming the Bloch-Siegert shift is negligible relative to the bandwidth of the pulse.

6.1.2 Slice Excitation by One-photon, Two-photon, and Frequency Modulation

Using the above procedure, the first three sets of pulses were designed to show that equal slice profiles can be created in multiple ways. The first set used a one-photon pulse, a two-photon with constant-$B_{1,z}$ pulse, and a one-photon with frequency modulation pulse corresponding to the two-photon pulse, all designed to excite the same slice profile. The one-photon pulse was a SLR pulse generated using SigPy.RF [28]. The SLR pulse was designed to have a time-bandwidth product of 3 and a duration of 3 ms. The corresponding slice-select gradient was set to have an amplitude resulting in a 5 mm slice-thickness. A rewinder gradient was added to give the standard excitation k-space trajectory.

The two-photon pulse was designed following Eq. [5.16] using a hard B_z pulse. As Eq. [5.16] shows, when exciting the two-photon resonance, the hard B_z pulse effectively scales $B_{1,xy}$ by $J_1\left(\frac{\gamma B_{1,z}}{\omega_z}\right)$, but otherwise excites the same slice profile. So, to get the same flip angle was the one-photon pulse, the same $B_{1,xy}$ pulse as the one-photon pulse was used, except that it was scaled by $1/J_1\left(\frac{\gamma B_{1,z}}{\omega_z}\right)$. To excite the two-photon resonance instead of the one-photon resonance, the frequency of the B_{xy} pulse was also decreased by ω_z. Note that two-photon resonances can be excited with the frequency of the B_{xy} pulse either increased or decreased by ω_z. To make the B_z pulse more easily implementable, $\phi = -\pi/2$ to make it a sine wave that starts at zero instead of a cosine wave. The initial phase of $\theta(t)$ was set to cancel out the resulting extra constant phase term given by $e^{-i(\frac{\gamma B_{1,z}}{\omega_z}\sin(\omega_z T+\phi)-n\phi)}$ in Eq. [5.16].

The one-photon frequency modulation pulse is a pulse where frequency modulation of the B_{xy} pulse imitates the effects of the B_z pulse. Specifically, in Eq. [5.11], the $e^{-i\theta(t)}$ term is set to be equal to the $e^{-i\gamma\int_t^T B_{1,z}(\tau)\cos(\omega_z\tau+\phi(\tau))d\tau}$ term from the two-photon pulse. $\theta(t)$ represents the phase/frequency modulation of the B_{xy} pulse. In this case, since the B_z pulse is a hard pulse, the integral can be directly evaluated, and so $\theta(t) = \frac{\gamma B_{1,z}}{\omega_z}(\sin(\omega_z T+\phi) - \sin(\omega_z t+\phi))$. Then, although there is no real B_z pulse, there is a fictitious one, so like for the two-photon pulse, $B_{1,xy}$ again needs to be multiplied by $1/J_1\left(\frac{\gamma B_{1,z}}{\omega_z}\right)$ to achieve the same flip angle as the original one-photon pulse. The major difference between the two-photon pulse and the frequency modulated pulse is that the two-photon pulse makes use of a real RF B_z field in the laboratory frame of reference while there does not exist one for the frequency modulated pulse in the laboratory frame of reference. As a result, despite its center frequency being offset by ω_z, the frequency modulated pulse actually has some frequency components at the Larmor frequency in the laboratory frame of reference while the two-photon pulse does not.

The designed pulses are shown in the first column of Fig. 6.3.

6.1.3 Slice Shifting with $\omega_{\mathbf{xy}}$, Constant B_z, or $\omega_{\mathbf{z}}$

The second set of pulses dealt with slice shifting for a two-photon pulse, and equal shifts were designed using $\theta(t), B_{DC,z}(t)$, or $\Delta\omega$ in Eq. [5.18]. All three pulses were the same two-photon pulse from the previous section, except shifted in position by the three methods. Setting $\theta(t) = \omega_{offset}t$, where ω_{offset} is some offset frequency, is the standard method of changing slice location by exciting a different local Larmor frequency along the slice-select gradient. From the theory, changing the frequency of the B_{xy} pulse in a two-photon pulse shifts the slice position of the two-photon pulse by the same amount as it would for the corresponding one-photon pulse.

Instead of changing the B_{xy} pulse frequency, changing the local Larmor frequencies by adding a uniform near-DC magnetic field, $B_{DC,z}(t)$, is another method that has been historically used to change the excitation location. Here, we set $B_{DC,z}(t)$ to a constant during the excitation and removed it for the rest of the pulse sequence to show that again, the two-photon slice position changes the same amount as a one-photon slice position would.

Finally, changing $\Delta\omega$ in Eq. [5.18] to change slice position is unique to two-photon pulses. Instead of changing the B_{xy} pulse frequency, we can change the B_z pulse frequency by an equal amount to shift the slice. Just like in the B_{xy} pulse frequency case, changing the B_z pulse frequency excites a different local Larmor frequency along the slice-select gradient. When $\Delta\omega$ is not insignificant compared to ω_z though, Eq. [5.18] shows that the Bessel function scaling factor changes. So, in this case, $B_{1,xy}$ was multiplied by $1/J_1\left(\frac{\gamma B_{1,z}}{\omega_z+\Delta\omega}\right)$ instead.

The designed pulses are shown in the first column of Fig. 6.4.

6.1.4 Amplitude-modulated $B_{1,xy}$ and $B_{1,z}$ Pulses

The third set of pulses was designed to show flexibility in choosing how the amplitude modulation can be split between $B_{1,xy}(t)$ and $B_{1,z}(t)$ based on Eq. [5.26]. Because of the additional assumption of slow variation of $B_{1,z}(t)$ relative to ω_z used for deriving Eq. [5.26], the pulse length was increased from 3 ms to 12 ms to allow for slower $B_{1,z}(t)$ variation. Alternatively, ω_z could be increased instead, but our experimental setup did not allow for it, which will be elaborated more upon in section 3.6. The first pulse in this set was the same as the second pulse from section 3.2, except with a 12 ms duration instead of 3 ms.

The second pulse in this set moved all the amplitude modulation from $B_{1,xy}(t)$ to $J_1\left(\frac{\gamma B_{1,z}(t)}{\omega_z}\right)$. That is, $B_{1,xy}(t)$ was made a time-invariant hard pulse with an amplitude equal to the maximum of $B_{1,xy}(t)$ from the first pulse and $J_1\left(\frac{\gamma B_{1,z}(t)}{\omega_z}\right)$ was set to be a scaled version of $B_{1,xy}(t)$ as a function of time from the first pulse with the same maximum value of $B_{1,z}(t)$ as in the first pulse. Because $J_1\left(\frac{\gamma B_{1,z}(t)}{\omega_z}\right)$ is a nonlinear function of $B_{1,z}(t)$, a bounded optimization function from SciPy [44] was used to find the values of $B_{1,z}(t)$ needed to give the correct values of $J_1\left(\frac{\gamma B_{1,z}(t)}{\omega_z}\right)$ at every time point. As a result, the product $B_{1,xy}(t)J_n\left(\frac{\gamma B_{1,z}(t)}{\omega_z}\right)$,

which is the total effective amplitude modulation of the two-photon pulse as shown in Eq. [5.26], was the same for the first and second pulses for all time.

The third pulse in this set was split into two halves. The first half had a hard pulse for $B_{1,xy}(t)$ while the second half had a hard pulse for $B_{1,z}(t)$. The product $B_{1,xy}(t)J_n\left(\frac{\gamma B_{1,z}(t)}{\omega_z}\right)$ was still the same for this pulse for all time, thus producing the same slice profile.

The designed pulses are shown in the first column of Fig. 6.5.

6.1.5 Multislice Excitation

Finally, for the fourth set of pulses, the earlier uniform B_z field was replaced by linearly spatially varying oscillating gradients. These oscillating gradients were added to a one-photon SLR pulse to demonstrate multislice excitation, and a spatially shifted version based on Eq. [5.31] was designed. The first pulse of this set was the same as the first pulse from the section Slice Excitation by One-photon, Two-photon, and Frequency Modulation, except with an additional oscillating gradient of frequency 2 kHz superimposed on the slice-select gradient. The AC or oscillating component of the gradient was chosen to have an amplitude of 1.5 times the amplitude of the DC or slice-select component of the gradient. By choosing this ratio of amplitudes and using a hard pulse for the gradients, $\frac{\gamma(\mathbf{G_{1,z}}\bullet\mathbf{r})}{\omega_z} = 1.5$ at the two-photon resonance locations, $\frac{\gamma(\mathbf{G_{1,z}}\bullet\mathbf{r})}{\omega_z} = 3$ at the three-photon resonance locations, and so on. This is because as we move to higher order resonances, ω_z, the frequency of the z-photon provided by the oscillating gradients, remains the same while $\mathbf{r}$, the position of the multiphoton resonance, gets multiplied by the number of z-photons involved as the local Larmor frequency changes with the DC component of the gradient and the resonance condition is at integer multiplies of ω_z offset from the isocenter Larmor frequency. A ratio of 1.5 was chosen because $J_1\,(1.5)$ and $J_2\,(3.0)$ are near the maximum points of $J_1(-)$ and $J_2(-)$ respectively. As a result, the two- and three-photon excitation bands are about 0.5 times as efficient as the one-photon band in terms of $B_{1,xy}$ strength. However, as noted before, these extra multiphoton bands are excited using the same $B_{1,xy}$ as the one-photon band, essentially being provided without extra RF energy deposition in a subject. The RF energy deposition from the oscillating gradients is negligible. To prevent errors from discontinuous gradients, ϕ was set to $-\pi/2$ for a sine wave instead of a cosine wave. With $\omega_z T = 12\pi$ radians, this gives an extra linearly spatially varying phase described by $e^{-i\frac{\gamma\mathbf{G_{1,z}}(T)\bullet\mathbf{r}}{\omega_z}\sin(\omega_z T+\phi)}$ in Eq. [5.31]. To remove this, the rewinder gradient after the pulse was adjusted to give the opposite linearly spatially varying phase.

The second pulse of this set was the same as the first pulse, except that the frequency of the B_{xy} pulse was changed. This pulse was made to demonstrate that with the spatially non-uniform $B_{1,z}$ field provided by the oscillating gradients, shifting the slices is not the same as in the earlier slice-shifting section. If the frequency of the B_{xy} pulse is changed, then the slices are shifted, but the flip angles of each slice do not remain the same because the Bessel function order and/or the argument to the Bessel function changes at each excited slice.

The third pulse of this set demonstrates that based on Eq. [5.31], a spatially uniform $B_{1,z}(t)$ term can change the spatial zero point of $\mathbf{G_{1,z}}(t)\bullet\mathbf{r}$, thus making it as if the oscillating gradients were shifted in space. When this is used together with the standard shift of the frequency of the B_{xy} pulse from the second pulse in this set, then the slices are shifted with preserved flip angles. To show that this can be implemented without the extra hardware of an additional B_z coil, the B_{xy} pulse frequency modulation equivalent was used instead. That is, $\theta(t)$ was used to provide the same effect as a uniform $B_{1,z}(t)$ term as described previously.

The designed pulses are shown in the first column of Fig. 6.6.

6.1.6 General Pulse Experimental Implementation Details

All experimental implementations were done on a GE 3T MR750w scanner (General Electric, Waukesha, WI, USA) with a liquid phantom, a GE 16-channel knee coil array for reception, and custom gradient echo sequences (GRE) written using the HeartVista platform (HeartVista, Inc., Los Altos, CA). The imaging plane was set to be perpendicular to the slice select axis to view slice profiles. An in-house built solenoid coil (18 inch diameter and 20 inch length with about 450 μH of inductance and 1 ohm of resistance) was used to generate a uniform B_z field [8] (Fig. 6.1). The coil was built from a pair of parallel 14 AWG wires wound 20 times around the outer surface of a PVC pipe and 20 times around the inner surface of the PVC pipe to connect to a Neutrik speakON connector on one side. Epoxy was used to stabilize the wires and to build a base for the coil, and a UL94 V-0 rated flame-retardant sound-dampening mat was wrapped around both the inner and outer sides of the coil for safety. Also for safety, fifteen baluns were made and placed on the cable connected to the coil to prevent coupling with the MRI scanner's RF transmit. B_z waveforms were generated by a Siglent SDG6022X arbitrary waveform generator (Siglent Technologies Co., LTD., Shenzhen, China) and amplified by an AE Techron 7224 amplifier (AE Techron, Inc., Elkhart, IN) in voltage-controlled current mode. The current from the amplifier was fed into the solenoid through a waveguide into the scanner room. To easily allow for a near-DC B_z pulse superimposed with the $B_{1,z}$ pulse, the coil was not tuned and matched. However, a high voltage 1000 pF chip capacitor (Manufacturer Product Number 222522K00102JQTAF9LM, Knowles Precision Devices, Norwich, United Kingdom) was placed in parallel with the coil near the output of the amplifier to reduce near-Larmor frequency noise and interference.

To synchronize the B_{xy} and B_z pulses, a 7.5-cm-diameter copper loop on a PCB was used to simultaneously probe the B_{xy} and B_z fields. It was connected to an oscilloscope and the loop was oriented almost entirely in line with the B_z coil such that the induced voltage on the loop would be similar for both B_{xy} and B_z despite the orders of magnitude difference in frequencies. The delay times of the pulse sequence trigger and the waveform generator were adjusted until the B_{xy} and B_z pulses overlapped in time with a precision of 1 μs. $B_{1,z}$ amplitudes were calibrated with a custom calibration program in HeartVista such that equivalent one- and two-photon pulses produced equal maximum signal for a 1D projection. In detail, the scanner was programmed to repeatedly output excitations with 1D

readouts using either just a standard one-photon B_{xy} pulse or a frequency-offset and scaled B_{xy} pulse with a trigger for the B_z pulse. The frequency-offset and scaled B_{xy} pulse was verified to produce no excitation without a simultaneous B_z pulse. For only the frequency-offset and scaled B_{xy} pulse, the pulse sequence triggered the waveform generator to generate corresponding frequency B_z waveforms to the amplifier, which produced current into the B_z coil (Fig. 6.2). The output voltage scaling of the waveform generator was increased until the maximum values of the Fourier transforms of the 1D readouts for both excitations were approximately equal to a precision of about 0.5%, limited by noise. Based on the fact that for the two-photon resonance, the B_{xy} pulse is effectively scaled by $1/J_1\left(\frac{\gamma B_{1,z}}{\omega_z}\right)$, the B_z max amplitude was determined to be about 0.2 mT at 25 kHz, which was limited by the amplifier. To prevent phase/frequency drifts between the scanner and the waveform generator, the waveform generator's clock was synchronized to the 10 MHz reference signal from the scanner. Although the amplifier was operated in voltage-controlled current mode, it was found that when used, the DC component of the B_z waveform from the waveform generator had higher gain than expected. So, it was experimentally reduced in magnitude compared to the AC component by decreasing it until the slice location for the second pulse in Fig. 6.4 was correct.

All $\omega_z/2\pi$ values used with the additional B_z coil were 25 kHz because the amplifier could not produce large enough $B_{1,z}$ amplitudes for use with practical $B_{1,xy}$ values at higher ω_z frequencies with this coil. Because of this relatively small ω_z value, the slice-select gradients were constrained to be relatively small in order to keep the frequency-offset B_{xy} pulses from exciting off-center slices in the phantom and fulfill the assumption that only a one or a two-photon resonance is significant. This translated to small time-bandwidth products or long RF pulses. Time-bandwidth products were also limited due to increasing peak $B_{1,xy}$ values with increasing time-bandwidth products. Since peak $B_{1,xy}$ values need to be scaled by $1/J_1\left(\frac{\gamma B_{1,z}}{\omega_z}\right)$ for two-photon pulses to achieve the same flip angle, small $B_{1,z}$ amplitudes make this scaling value large and potentially impractical.

6.2 Results

6.2.1 Slice Excitation by One-photon, Two-photon, and Frequency Modulation

Fig. 6.3 shows the simulations and experimental results of the pulses described in the corresponding methods section. The first row corresponds to the one-photon pulse, the second row corresponds to the two-photon pulse, and the third row corresponds to the frequency-modulated one-photon pulse. The first column plots the excitation portion of the pulse sequence, the second column plots the simulated results of the excitation based on Eq. [5.1], and the third column shows the slice profile imaged via a plane perpendicular to the slice-select axis. A close-up view of a part of the excitation pulse sequence denoted by

the dotted red lines is provided in the right side of the first column, and a line plot of the intensity across the center of the slice profile image is also provided in the third column.

As shown in Fig. 6.3, one-photon, two-photon, and frequency-modulated one-photon pulses produce the same slice-selective excitation when designed to be equivalent. The simulated and experimental slice profiles appear as expected. The slice profiles are not too sharp, as expected, because of the small time-bandwidth product of only 3. While the scaling on most of the plots are the same, the $|B_{xy}|$ values for the two-photon and frequency-modulation pulses are larger by a factor of $\frac{1}{J_1\left(\frac{\gamma B_{1,z}}{\omega_z}\right)} = \frac{1}{J_1\left(\frac{42.58(200)}{25000}\right)} = 5.96$ by design to achieve the same flip angle as the one-photon pulse. If larger B_z values could be achieved, $\frac{1}{J_1\left(\frac{\gamma B_{1,z}}{\omega_z}\right)}$ could be as low as 1.72.

6.2.2 Slice Shifting with $\omega_{\mathbf{xy}}$, Constant B_z, or $\omega_{\mathbf{z}}$

Fig. 6.4 shows the simulations and experimental results of the two-photon pulse from Fig. 6.3, except shifted in position by three different methods as described in the corresponding methods section. The first row corresponds to shifting via changing ω_{xy}, or equivalently a linear $\theta(t)$. The second row corresponds to shifting via $B_{DC,z}(t)$, and the third row corresponds to shifting via changing ω_z. The columns are analogous to Fig. 6.3. When a two-photon pulse is used, it can be shifted by a change in ω_{xy}, the addition of a constant B_z,or a change in ω_z. The changes in ω_{xy} and ω_z are small compared to ω_{xy} and ω_z, so the differences in the plots are a little difficult to spot. However, in the close-up views of the pulse sequences, the phases can be seen to slightly differ. For the constant B_z row, note that the B_z subplot has a slight negative offset relative to the dotted lines representing zero field.

As shown in Fig. 6.4, the three ways of shifting the slice can produce equivalent shifts.

6.2.3 Amplitude-modulated $B_{1,xy}$ and $B_{1,z}$ Pulses

Fig. 6.5 shows the simulations and experimental results of two-photon SLR pulses with a time-bandwidth product of 3 and a duration of 12 ms, as described in the corresponding methods section. The first row corresponds to the pulse with amplitude modulation fully in the B_{xy} pulse, the second row corresponds to the pulse with amplitude modulation fully in the B_z pulse, and the third row corresponds to the pulse with amplitude modulation in both the B_{xy} and B_z pulses. Making the pulses have longer durations allows the assumption that the modulation of the B_z pulses is slow compared to the frequency ω_z to be better satisfied. Given the proper equipment, ω_z could have been increased by a few times instead of the duration of the pulse. All three pulses have essentially the same slice profile, but in the simulated profile in the second row, some extremely slight stopband ripple can be seen. These ripples likely disappear with better satisfied assumptions. They likely do not appear on the experimental images because the signal is too small and may have relaxed away.

6.2.4 Multislice Excitation

Fig. 6.6 shows the simulations and experimental results for the multislice excitation pulses described in the corresponding methods section. The first row demonstrates the principle of getting free unequal slices by taking the base one-photon pulse from Fig. 6.3 and adding an oscillating gradient waveform to the slice select gradient. This creates a spatially varying $B_{1,z}$ field. From the combination of the effects of a slice-select gradient and a spatially varying $B_{1,z}$ field, excitation occurs whenever multiphoton resonance conditions are met. Unlike in the previous examples, here we wanted multiple multiphoton resonances to be in the field of view instead of just one. The isocenter has a one-photon resonance. The two bands immediately adjacent are two-photon resonances, the two after that are three-photon resonances, etc. For the first pulse in Fig. 6.6, despite B_{xy} being exactly the same as the first pulse in Fig. 6.3, many extra excitation bands are created. As shown in the second pulse in the second row, however, shifting ω_{xy} does not equally shift all of the pulses. At the isocenter, because there is no $B_{1,z}$ field, there can only ever be a one-photon resonance. This can be fixed by either adding a uniform $B_{1,z}$ field such that the isocenter can have multiphoton resonances, or by using the corresponding frequency modulation of the B_{xy} pulse. The final pulse in Fig. 6.6 goes the frequency modulation route. Experimentally, however, the shifted center band does not quite reach the expected amount of excitation. This is likely due to the gradient amplitude at this position not being the expected value, perhaps due to gradient nonlinearity. In the image reconstruction, no gradient nonlinearity corrections were done, and based on the slice positions of the simulation vs. the image, it seems that the gradient may indeed be different from expected.

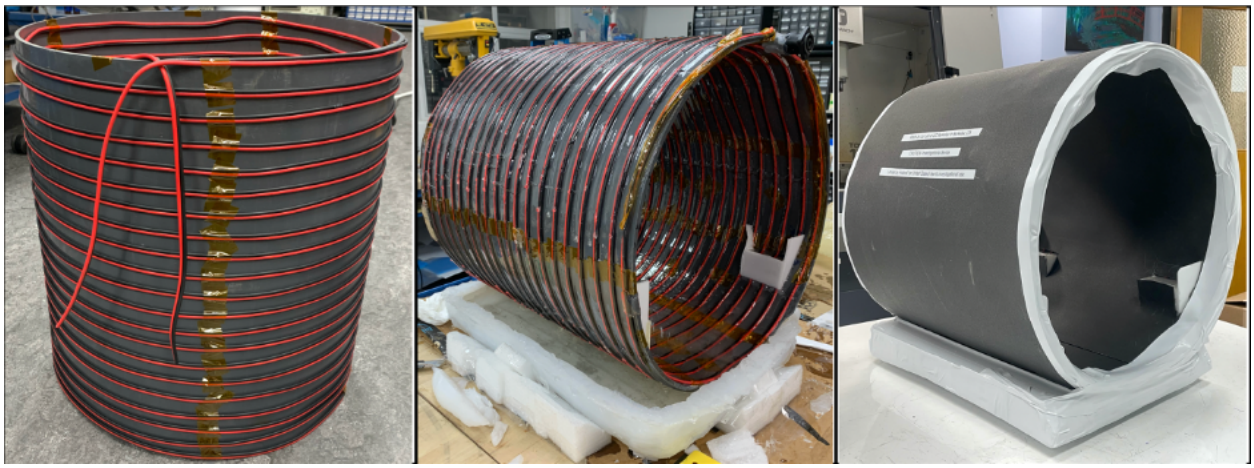

Figure 6.1: **B_z Coil Construction.** Left: Parallel wires winding the inner and outer surfaces of a 18 inch diameter and 20 inch length PVC pipe. Middle: Epoxy applied to stabilize the wires and base being made for the coil. Right: Coil wrapped with a flame-retardant sound-dampening mat.

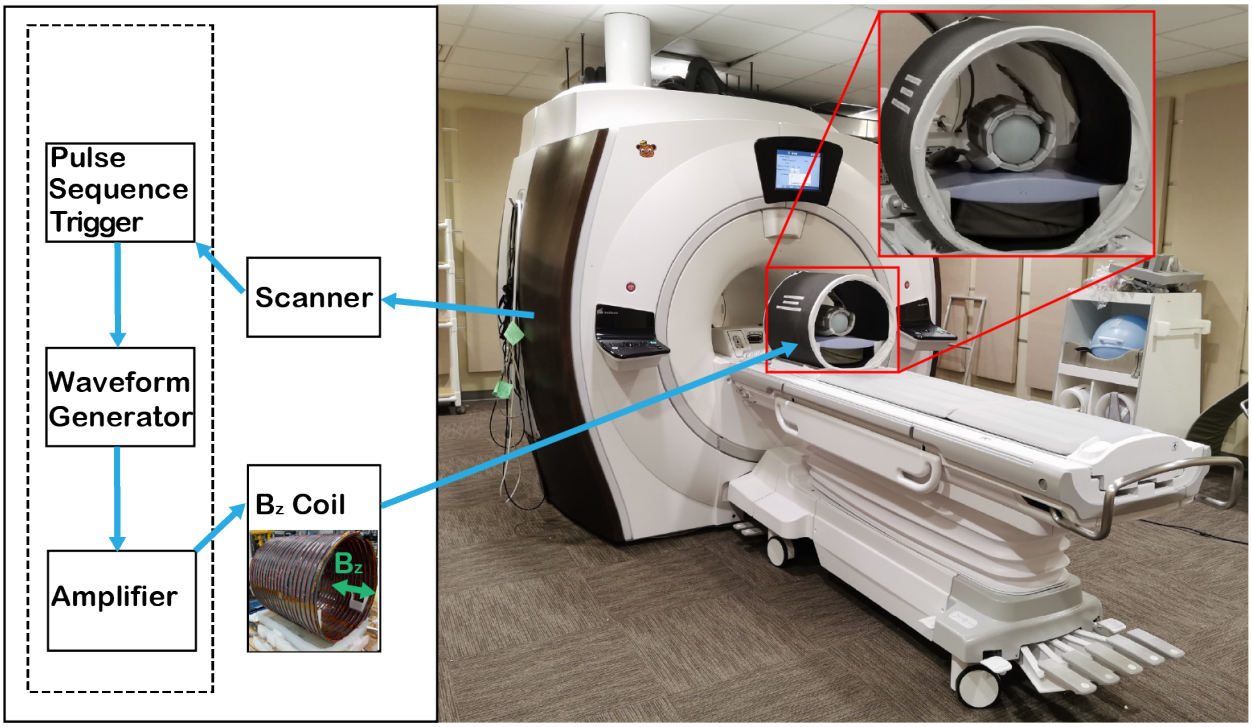

Figure 6.2: **MRI System Setup with a B_z Coil.** For experiments that need a uniform B_z field, the pulse sequence triggers a waveform generator. The output of the waveform generator gets amplified by an amplifier in voltage-controlled current mode, and the current goes to a big solenoid, which produces a magnetic field in the same direction as B_0. A smaller picture of the solenoid before it was encased is shown on the left. A knee coil for reception wraps around a phantom inside the solenoid. The body coil is used for B_{xy} transmit.

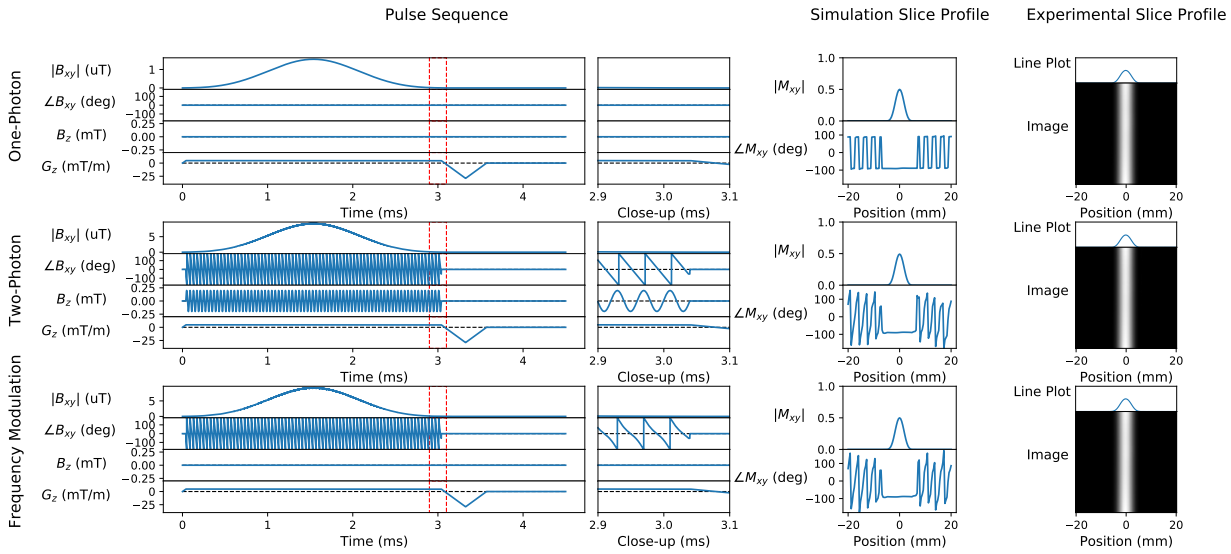

Figure 6.3: **Waveforms, Simulations, and Results for Corresponding One-photon, Two-photon, and Frequency Modulation Pulses.** The excitation pulse sequence, simulation, and experimental results are shown for corresponding one-photon, two-photon, and frequency modulated one-photon pulses. The dotted red lines indicate where the close-up view of the pulse sequence is. From the close-up, the frequency modulation of the final pulse can be more easily seen. All pulses are 5 mm slice thickness and have a time-bandwidth product of 3. The profiles are the same in both simulation and experiment.

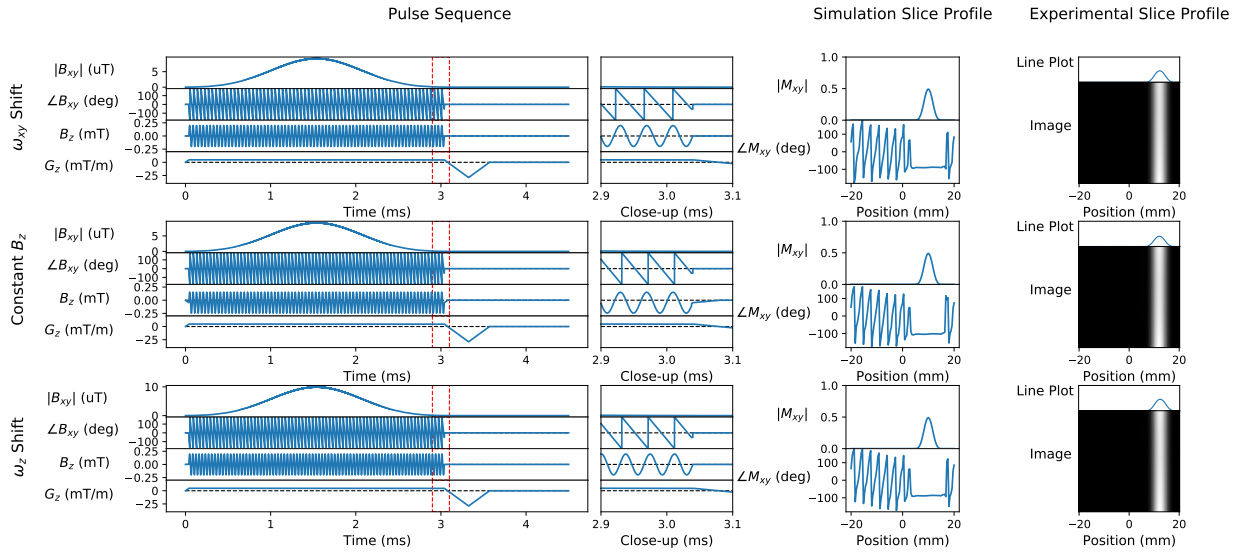

Figure 6.4: **Waveforms, Simulations, and Results for Corresponding Slice Position Shifts with omega$_{xy}$, Constant B$_z$, or omega$_z$.** The excitation pulse sequence, simulation, and experimental results are shown for equivalent slice shifts using a change in ω_{xy}, a DC B_z field, and a change in ω_z. The dotted red lines indicate where the close-up view of the pulse sequence is. From the close-ups, the first pulse has a slightly slower B_{xy} phase variation, the second pulse has a slight negative DC offset with a ramp at the end in the B_z field, and the third pulse has a slightly higher ω_z. The first pulse uses a slower phase variation because ω_{xy} was originally shifted to be lower than the Larmor frequency for this two-photon excitation. So, to increase the slice position, an increase in ω_{xy} means a slower phase variation in the Larmor frequency rotating frame.

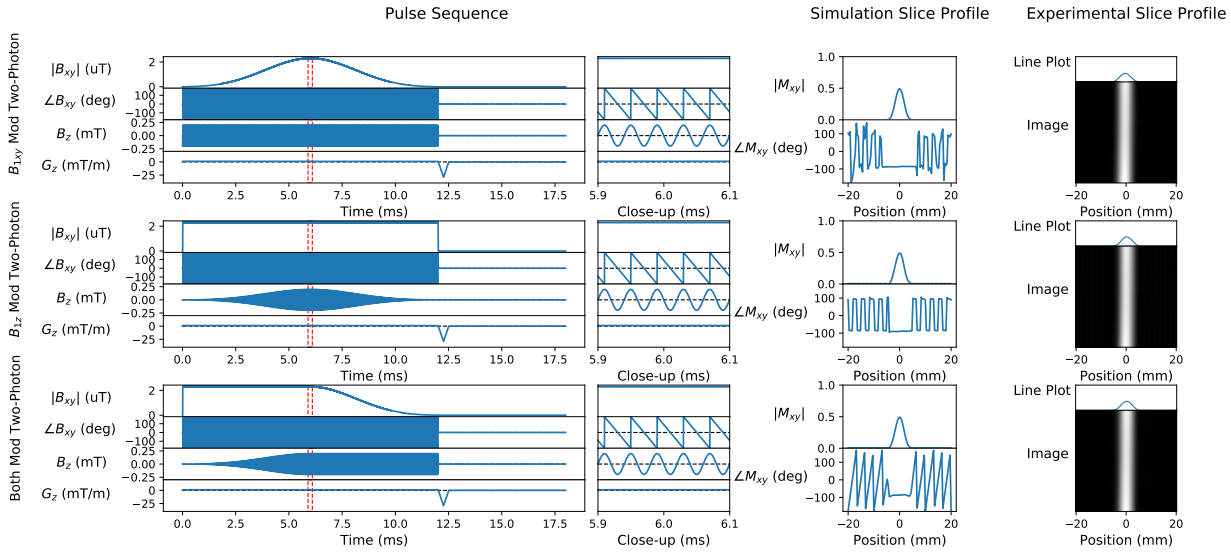

Figure 6.5: **Waveforms, Simulations, and Results for Corresponding Pulses Using Modulation in $\mathbf{B_{1,xy}}$, $\mathbf{B_{1,z}}$, or Both.** The excitation pulse sequence, simulation, and experimental results are shown for equivalent two-photon pulses with modulation in $B_{1,xy}$, $B_{1,z}$, or both. With the longer pulse duration, the oscillations on $B_{1,z}$ are no longer easily visible, thus better satisfying the assumption that modulation on $B_{1,z}$ is slow compared to ω_z. The dotted red lines indicate where the close-up view of the pulse sequence is. In the close-ups, it can be seen that B_z is still indeed oscillating, and that ω_{xy} is still offset by the same amount.

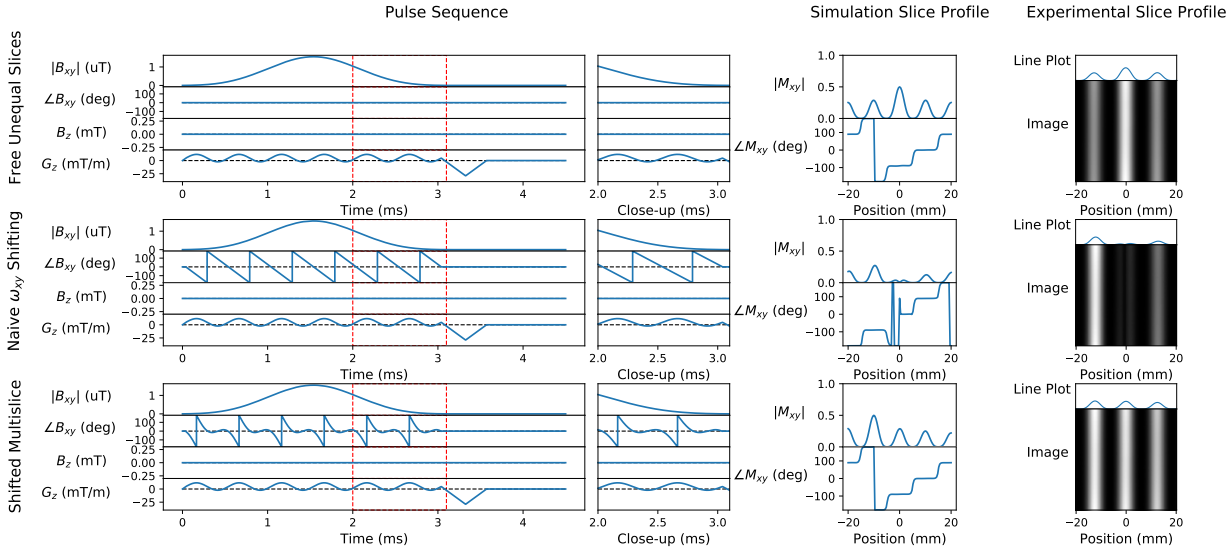

Figure 6.6: **Oscillating Gradients Generate Free Extra Slices, Which Should Be Shifted Using Both a Change in omega$_{xy}$ and Frequency Modulation or a B$_{1,z}$ Pulse.** The excitation pulse sequence, simulation, and experimental results are shown for multislice pulses. The first row is the same pulse from the first row of Fig. 6.3, but with the addition of an oscillating gradient to produce extra bands for free. The second row shows that simply changing ω_{xy} does not uniformly shift the bands. To properly shift the bands, a uniform $B_{1,z}$ or the equivalent frequency modulation of B_{xy} as used here is needed. The shifting is not perfect, however, as the gradients in this part of the phantom may be smaller than expected.

Chapter 7

In Vivo Multiphoton Excitation

So far, the only in vivo scans performed with multiphoton excitation were done using oscillating gradients. However, the oscillating gradients do not provide a uniform $B_{1,z}$ field and are limited in frequency to the low kHz range, especially for a whole body scanner. In this chapter, we describe in vivo scans of a human brain with two-photon excitation using an additional homogenous $B_{1,z}$ coil operating at 25 kHz. Standard one-photon scans with flip angles designed to be equivalent are provided for comparison.

7.1 Methods

Under informed consent and procedures approved by our institution's IRB, a healthy volunteer was scanned with the same GRE sequences as the phantom experiments to show the in-plane images resulting from the selective excitation for single- and two-photon excitation. The parameters of the in vivo scans were: TR/TE = 200/4.9 ms, FA = 20°, 30°, or 40°, FOV = 220x220 mm^2 for the axial slice and 256x256 mm^2 for the sagittal and coronal slices, matrix = 256x256, 1 slice of 5-mm thickness, 62.5-kHz readout bandwidth, 54-sec scan time. For the two-photon pulses, 25 kHz $\omega_z/2\pi$, -25 kHz offsets to $\omega_{xy}/2\pi$, 0.2 mT $B_{1,z}$ amplitude, $B_{1,xy}$ was 5.96 times larger than for the corresponding one-photon pulses.

7.2 Results

Using the same one-photon and two-photon pulses as in Fig. 6.3, Fig. 7.1 shows the in-plane results of the one-photon and two-photon pulses in vivo in three different orientations. Difference images are also given as one-photon minus two-photon for each pair. There is significant shading in the images because the same knee coil for reception used for the phantom experiments was wrapped around the head, and because the coil was designed for a knee, the coverage of the head was not complete. No significant differences between the images are visually observed for this set of parameters, but there are still some differences observed in the subtraction images. The subtraction images are red for locations where one-photon was

Image	SNR
One-Photon Axial (20° FA)	35.0
Two-Photon Axial (20° FA)	34.5
One-Photon Axial (30° FA)	44.8
Two-Photon Axial (30° FA)	42.7
One-Photon Axial (40° FA)	50.8
Two-Photon Axial (40° FA)	48.1
One-Photon Sagittal (20° FA)	53.7
Two-Photon Sagittal (20° FA)	49.7
One-Photon Sagittal (30° FA)	67.0
Two-Photon Sagittal (30° FA)	63.4
One-Photon Sagittal (40° FA)	72.8
Two-Photon Sagittal (40° FA)	71.6
One-Photon Coronal (20° FA)	72.4
Two-Photon Coronal (20° FA)	70.4
One-Photon Coronal (30° FA)	89.2
Two-Photon Coronal (30° FA)	88.2
One-Photon Coronal (40° FA)	98.0
Two-Photon Coronal (40° FA)	96.0

Table 7.1: White Matter SNR for In Vivo Scans

larger and blue for where two-photon was larger. Linear registration in the Fourier domain was applied before subtraction in the image domain. While these differences are of similar order of magnitude to the background noise, there is likely some slight systematic error in the flip angle calibration for the two-photon scans. Based on how the tissue signal generally increases with flip angle for these parameters, the two-photon scan flip angles appear to be consistently slightly smaller than the one-photon scan flip angles. SNR values were calculated for white matter regions of interests by taking the mean of at least 300 white matter voxels and dividing by the standard deviation of 10,000 background voxels. The results are tabulated in Table 7.1. The two-photon SNR values are consistently slightly lower for all orientations and flip angles, which further implies some flip angle systematic error. This error likely arises from the combination of the calibration method of matching maximum signal strengths of 1D projections and some slight inhomogeneity in the B_z coil. The maximum signal may have come from a blood vessel closer to the coil, where the B_z field may be larger. An optimized, more homogenous B_z coil is the subject of future work. Otherwise, the one-photon and two-photon images appear to be of similar quality.

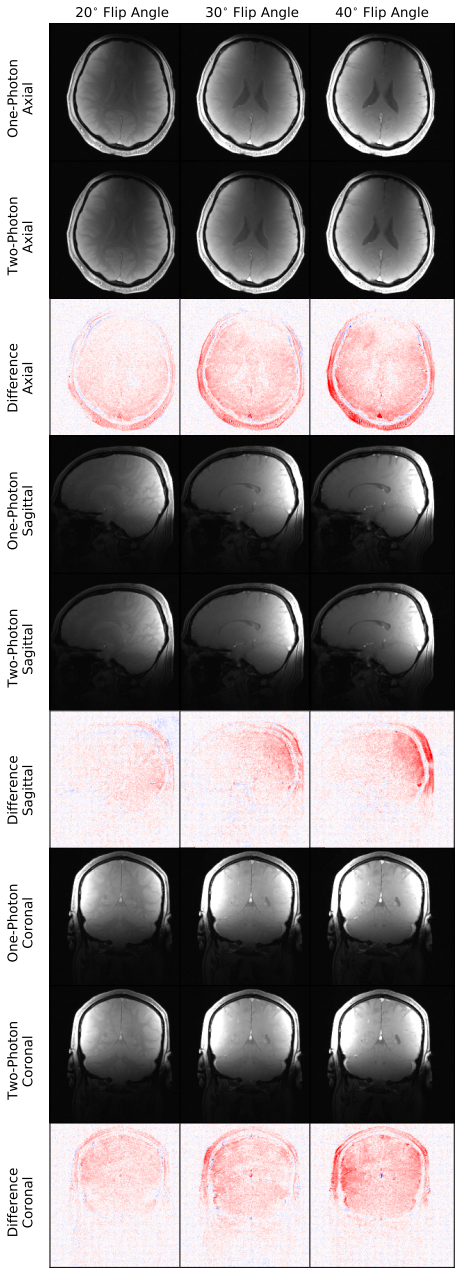

Figure 7.1: **In Vivo One- and Two- Photon Selective Excitations Produce Similar Images When Designed to be Equivalent.** The same one- and two-photon selective excitation pulses from Fig. 6.3 were used for slice-selective in-plane imaging of a healthy volunteer. Three different orientations are shown for three different flip angles. The maximum flip angle was limited by the peak $B_{1,xy}$ amplitude required for the given pulse parameters and maximum $B_{1,z}$ amplitude available. The sagittal and coronal images were cropped to remove some empty space. Difference images are red for greater signal in one-photon scans and blue for greater signal in two-photon scans.

Chapter 8

Zero Dead Time Earth's Field NMR using Two-Photon Excitation

In this chapter, we take a detour into multiphoton excitation for ultralow field NMR/MRI. Ultralow field NMR/MRI presents many potential opportunities such as reduced cost, reduced chemical shifts, reduced susceptibility effects, increased portability, long liquid relaxation times, new contrasts, the ability to image through thin metal, and high-resolution J-coupling measurements [23]. It is also a very interesting regime to study where applied time varying fields such as gradients and B_1 fields can easily become comparable in magnitude to the B_0 field. For gradients, this presents challenges in that unless the gradients are very small, concomitant fields cannot be ignored [45]. For spatially uniform fields such as B_1 fields, we can view this regime not as detrimental, but rather, as advantageous. Since SAR generally scales with $(fB_1)^2$ [18], limits are nearly non-existent, and with higher B_1 field strengths, we can take advantage of physical phenomena that may otherwise not be as practical at standard B_0 fields. One example is two-photon excitation with a single frequency at half the Larmor frequency. Although half-frequency two-photon excitation has been used for simultaneous transmit and receive in NMR at 9.4 T [31], it relies on relatively intense RF fields and is difficult to extend to imaging with large sample sizes. As described earlier in this dissertation, two-photon excitation can be used for imaging, but to make it more practical, multiple frequencies whose sum or difference equaled the Larmor frequency were used instead. So, in this work, we developed half-frequency two-photon excitation with a B_0 of the Earth's magnetic field, which is approximately 50 μT. By using a transmit frequency of about 1 kHz and a receive frequency of about 2 kHz, we built a directly connected signal pipeline from the transmitter to the receiver without any intentionally non-linear elements in between. Using filters to prevent the transmitted signal from saturating the receiver, we could transmit and receive at the same time. Figure 8.1 shows a diagram of this. While some harmonic distortion in the circuit prevented us from fully separating the transmit from the received signal during excitation, the always connected and unsaturated receive circuitry allowed us to completely eliminate receiver dead time, which can often be quite long, especially at low frequencies.

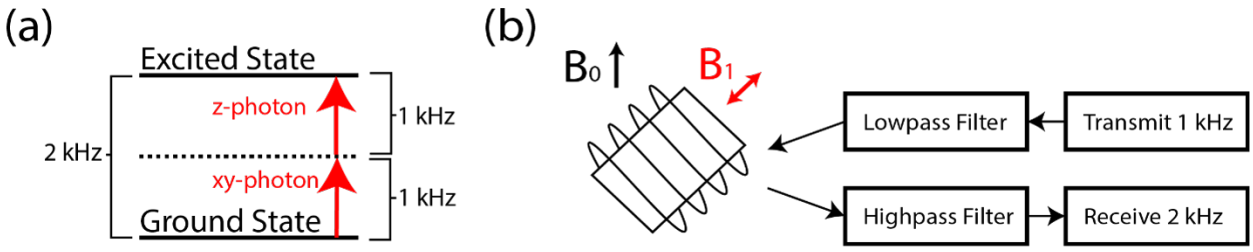

Figure 8.1: **Two-photon excitation at Earth's field.** a) Two 1 kHz photons with different polarizations can be absorbed to excite a 2 kHz energy gap in two-photon excitation. b) Both xy- and z-polarizations can be provided by a coil angled 45 degrees with respect to the B_0 field. When the B_0 field is the Earth's magnetic field, it corresponds to a Larmor frequency of about 2 kHz, and filters can be used to isolate a 1 kHz transmit for two-photon excitation from a Larmor frequency receive.

8.1 Methods

A homebuilt prepolarized Earth's field spectrometer was built following a combination of techniques from Michal [30] and Trevelyan [43]. For pulse programming, a Matlab script via an ASIO interface was used to control a RME ADI-2 Pro FS (RME, Germany) synchronized to an Analog Discovery 2 (Digilent, USA). The RME ADI-2 Pro FS was used to transmit pulses and acquire data, while the Analog Discovery 2 was used to provide control signals for various relays related to prepolarization. Figure 8.2 shows a block diagram of the overall system. To implement simultaneous two-photon excitation and reception, active lowpass and highpass filters were designed. Figure 8.3 shows schematics and simulations for the filters. The lowpass filter was connected to the output of the RME ADI-2 Pro FS to filter out noise and harmonic distortion in the transmit waveform. The output of the lowpass filter was coupled to the transmit/receive coil with a capacitor. The voltage across the transmit/receive coil was connected to a unity gain buffer, which was then connected to a highpass filter to filter out the transmit frequency and keep the Larmor frequency signal. The output of the highpass filter was connected to the input of the RME ADI-2 Pro FS. Figure 8.4 shows these more detailed connections.

8.2 Results

Figure 8.5 shows the result of a spin echo sequence with and without the prepolarization power supply turned on, thus giving results with and without NMR signal. When the prepolarization is used, FIDs can be seen directly after the 90- and 180-degree pulses. The FID

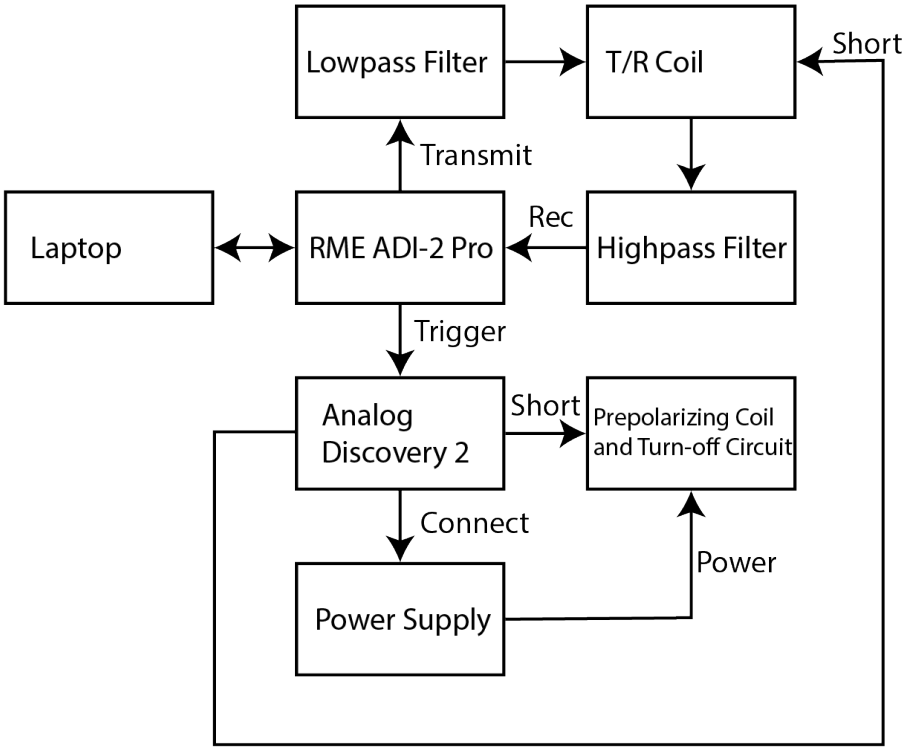

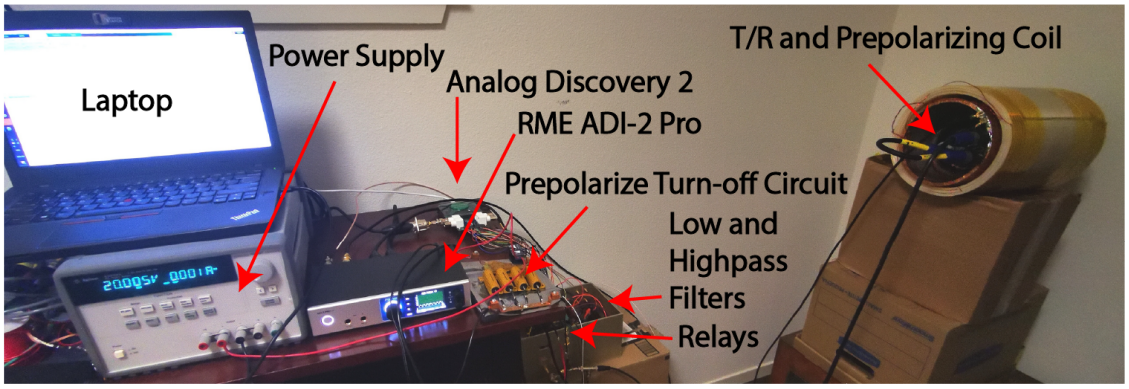

Figure 8.2: **System block diagram.** A laptop generates transmit waveforms and processes received data from an audio interface, RME ADI-2 Pro. This audio interface continuously outputs through a lowpass filter and receives data through a highpass filter throughout the pulse sequence. Using a second output channel, the RME ADI-2 Pro triggers an Analog Discovery 2 to handle digital triggers for prepolarization. The T/R coil is only shorted during prepolarization and its associated turn-off to protect the electronics from a very large and sharp induced voltage.

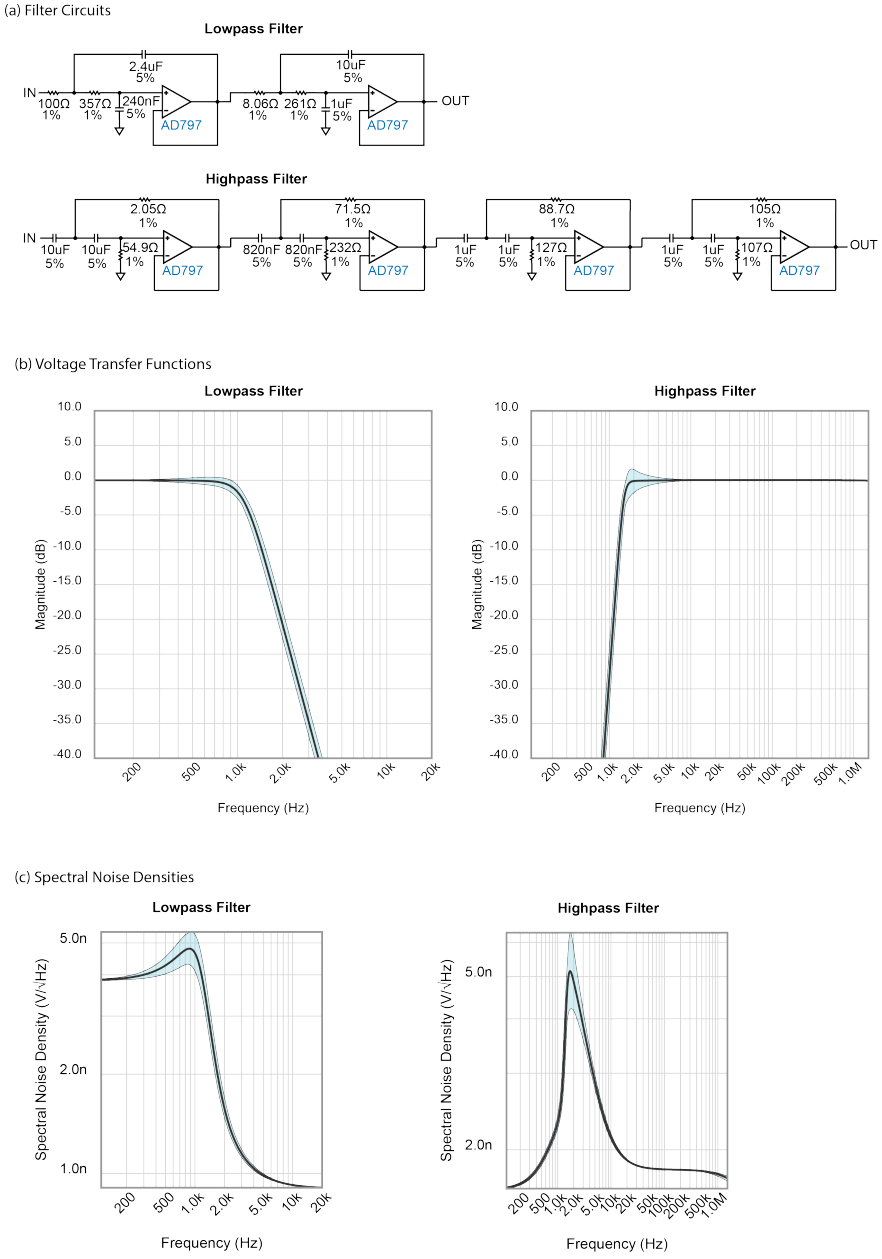

Figure 8.3: **Filters.** a) A 4th order lowpass filter was designed using Analog Devices' filter wizard to filter out noise and distortion from the already very high quality RME ADI-2 Pro output, which under ideal conditions has a 2nd harmonic better than -120 dBc at 1 kHz. b) An 8th order highpass filter was designed to filter out the transmit frequency and prevent saturation in the receiver. This worked for our transmit voltage levels, but higher order filters could be designed if needed for higher transmit voltages. High capacitances and low resistances were chosen for low voltage noise.

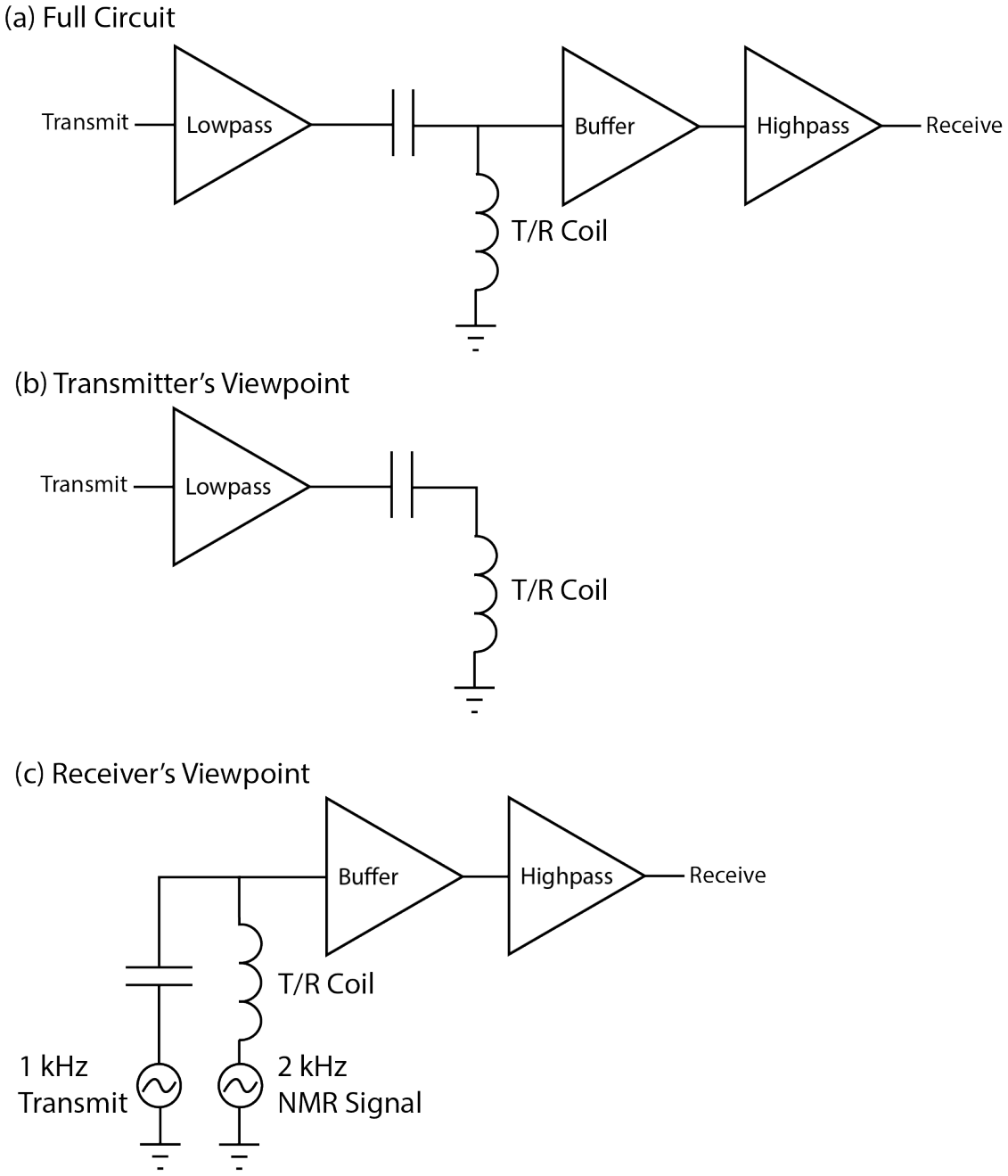

Figure 8.4: **Filter to coil connections in detail.** a) The output of the lowpass filter was capacitively coupled to the T/R coil. A high impedance unity gain buffer was placed before the highpass filter to prevent the filter from affecting the coil and vice versa. b) Due to the high impedance buffer, the transmit side only "sees" a series capacitor and a coil. c) With an ideally zero output impedance for the lowpass filter, the receive side only "sees" a parallel capacitor and coil with two series voltage sources: the transmit source and the NMR signal. The transmit gets filtered before the final ADC.

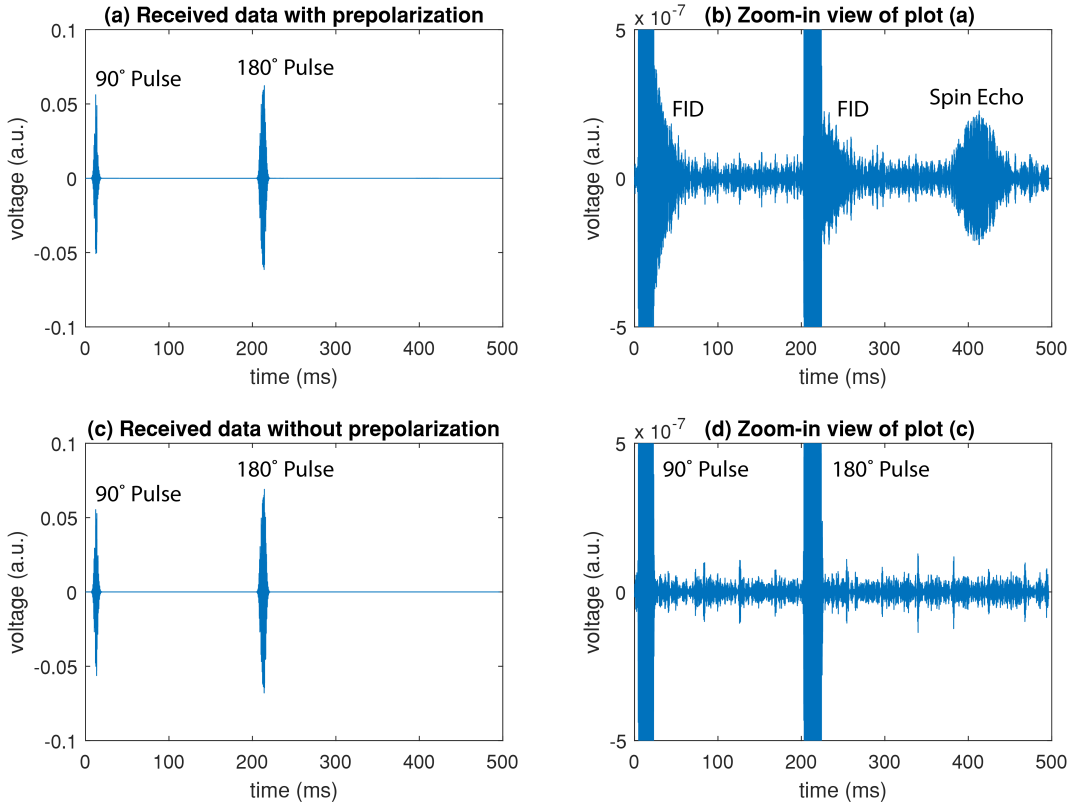

Figure 8.5: **FIDs and Spin Echo.** A drinking water bottle was used as a sample and pulse sequences with and without the prepolarization power supply turned on were executed 512 times each. The resulting data was averaged, digitally bandpass filtered, and displayed. a) Large second harmonic distortion is still seen when the 90- and 180-degree pulses are transmitted. b) Scaling the y-axis reveals FIDs and a spin echo, with the FIDs directly after the pulses with no delay. c) Without prepolarization, the transmit distortion is the same as in (a). d) Without prepolarization, the NMR signals are gone.

after the 180-degree pulse is likely from excited off-resonant spins. Without prepolarization, only the second harmonic distortion from the excitation pulses is observed.

8.3 Discussion and Conclusions

We have achieved zero dead time NMR at Earth's field by separating the transmit and receive frequencies and using filters to isolate them. These filters were implemented using op amps, resistors, and capacitors instead of inductors and capacitors because inductors for this frequency range were found to be overly bulky, have low Q factors, and easily pick up external interference signals. Although op amps and resistors introduce noise into the circuit, this was mitigated by proper choice of op amps and low resistance values. Unfortunately, the circuit still provided decent second harmonic distortion that made us unable to acquire signal during transmit. The cause of this will be investigated in future work. Improving the SNR of the base Earth field NMR setup by shimming the B_0 field and moving it out of a noisy apartment closet may also help with this.

Although prepolarization can help overcome the low thermal polarization of ultralow field NMR/MRI, the prepolarization step is very time consuming, and it is still difficult to get a very large signal. In the future, we would like to apply this technique to hyperpolarized studies such as with hyperpolarized Carbon-13. Along with long liquid relaxation times and high potential field homogeneity at low field, zero dead time/simultaneous transmit and receive could increase SNR and potentially reveal any ultrashort T_2 signals.

Chapter 9

Discussion and Conclusions

9.1 Summary

We present here a general approach for analyzing and implementing multiphoton MRI under a classical framework. The approach unifies one-photon and multiphoton excitation under the same mathematical framework. The approach is validated with both simulation and experiments.

The multiphoton interpretation predicts a type of excitation that occurs even when the RF field has no frequency components near the Larmor frequency. In this dissertation, we have provided ways to determine the effects of such excitations. With the multiphoton interpretation, true-resonance conditions are established, and with this knowledge, extensions for shaped pulses and nonlinear effects such as the Bloch-Siegert shift and adiabatic pulses follow.

9.2 Future Directions

Although two-photon pulses were mainly used as examples, the theory shows that there are direct extensions to higher-order multiphoton pulses. Fig. 6.6 exemplifies this and shows that by allowing non-uniform B_z fields, more spatially complex excitation can be achieved with no increase in B_{xy} amplitude or duration. Although the example shown here may not yet be useful for simultaneous multislice [24, 41] applications due to the non-uniform flip angles between slices, multiphoton parallel transmit and higher channel-count spatial encoding fields would be able to compensate for the non-uniformity. When designing hardware for these applications, it would be best to increase ω_z and $B_{1,z}$ as much as practical to satisfy the assumptions made in the theory section and to remove the practical constraints described in Chapter 5. We expect that this may be best done with $\omega_z/2\pi$ in the hundreds of kHz and arrays of smaller coils.

For a multiphoton pulse, the ability to transfer modulation to a B_z pulse may be useful in various more niche circumstances. When designing a new scanner from the ground up,

shimming coils or other coils that generate B_z fields to traditionally compensate for drifts in the B_0 field may add modulation to their duties, and in return, the traditional RF transmit signal chain may be reduced in complexity. In an extreme case, the traditional B_{xy} RF could simply only need to turn on and off, potentially simplifying a low-cost, ultralow field scanner. Besides simplifying the RF signal chain, if a transmit coil has difficulty reaching large B_{xy} values for high nutation frequencies, such as for imaging nuclei with very low gyromagnetic ratios, the ability to not care about modulation and required bandwidth allows a coil designer to optimize for Q factor as much as possible, increasing transmit coil efficiency to the limit. While this may not be relevant for high field scanners where Q factors limited by sample loss provide large bandwidths, ultralow field scanners where the Q factor is limited by the coil loss and required imaging bandwidth may find benefits.

Because multiphoton excitation applies RF fields with frequencies significantly shifted from the Larmor frequency, one compelling application of multiphoton MRI is simultaneous transmit and receive via frequency isolation. Simultaneous transmit and receive MRI has been implemented in other ways [10, 20, 42, 34], and provides the advantage of high imaging efficiency without dead time and high signal-to-noise ratio with minimal T_2 and T_2* decay, especially useful for imaging short-T_2 species. However, as Brunner et al. also noted for sideband excitation [7], such a scheme with multiphoton excitation may be most practical at low main magnetic field strengths. This is because the efficiency of multiphoton excitation depends on an absolute, not relative, offset from the Larmor frequency. A simultaneous transmit and receive scheme would require filters to separate the transmit frequency from the received frequency. Separating a 100 kHz and 50 kHz transmit and receive would be much easier than separating a 100.1 MHz and 100.05 MHz transmit and receive. Furthermore, at low fields, SAR from the decreased excitation efficiency is a smaller concern, and larger RF fields are easier to produce at lower frequencies.

To address the filter challenge at high fields, we are attempting to implement a mixer-first receiver architecture (for example, see [2, 3, 32, 21]) that would allow for separation of very close RF frequencies by filtering after initial down-conversion to baseband frequencies. In a standard receiver architecture with a low-noise amplifier before the mixer, the low-noise amplifier may easily become saturated by the strong transmit signals. By first filtering out the transmit signals with a very linear passive mixer instead, low-noise amplifier saturation is less of a concern.

Multiphoton MRI offers a new way to explore novel contrast for MRI. While, post multiphoton excitation, the magnetization evolves similarly as in single-photon excitation, the multiphoton excitation pulses can alter signal evolution during excitation. For example, excitation RF is known to affect relaxation rates such as with $T_{1\rho}$ and the recently described relaxation along a fictitious field [26]. Multiphoton excitation provides a new way to manipulate multiple RF waveforms and sample various interaction time scales. For example, a $B_{1,z}$ field could be chosen to be in sync with biological or chemical processes of interest and impact the corresponding MRI signal. The choice of multiphoton excitation RF frequencies could also alter the effect of magnetization transfer and chemical-exchange saturation transfer. The in vivo scans described in this dissertation do not show significant differences

between one- and two-photon excitation. However, in other experiments not described in this dissertation, under certain parameters, some small structures have shown some interesting results. We are still investigating the cause and whether or not these interesting results are just artifacts.

As gradient [27, 13] and traditional RF coils gain more channels and spatial-temporal flexibility, much more can be achieved using multiphoton MRI to encode spatial, spectral and temporal information.

Chapter 10

Appendix

10.1 General multiphoton excitation with one xy-photon

In the phase-modulated rotating frame, we have

$$B_{z,eff} = B_0 - \frac{\omega_{xy}}{\gamma} \tag{10.1}$$

$$B_{x,eff} = B_{1,xy} \cos\left(\frac{\gamma B_{1,z}}{\omega_z} \sin(\omega_z t)\right) \tag{10.2}$$

$$B_{y,eff} = B_{1,xy} \sin\left(\frac{\gamma B_{1,z}}{\omega_z} \sin(\omega_z t)\right) \tag{10.3}$$

Eq. [10.2] and Eq. [10.3] can be combined to form

$$B_{xy,eff} = B_{1,xy} \cos\left(\frac{\gamma B_{1,z}}{\omega_z} \sin(\omega_z t)\right) + iB_{1,xy} \sin\left(\frac{\gamma B_{1,z}}{\omega_z} \sin(\omega_z t)\right) = B_{1,xy} e^{i\frac{\gamma B_{1,z}}{\omega_z} \sin(\omega_z t)} \tag{10.4}$$

With J_n representing the Bessel function of the first kind with integer order n, the generating function of the Bessel function of the first kind is

$$e^{\frac{x}{2}\left(z - z^{-1}\right)} = \sum_{n=-\infty}^{\infty} J_n(x) z^n \tag{10.5}$$

Let $z = e^{i\omega_z t}$, then $i \bullet sin(\omega_z t) = \frac{1}{2}(z - z^{-1})$. Eq. [10.1] becomes

$$B_{1,xy} e^{i\frac{\gamma B_{1,z}}{\omega_z} \sin(\omega_z t)} = B_{1,xy} e^{\frac{\gamma B_{1,z}}{2\omega_z}\left(z - z^{-1}\right)} = B_{1,xy} \sum_{n=-\infty}^{\infty} J_n\left(\frac{\gamma B_{1,z}}{\omega_z}\right) e^{in\omega_z t} \tag{10.6}$$

This is known as a Jacobi-Anger expansion. From Eqs. [10.1, 10.6], resonances occur whenever

$$\omega_{xy} = \gamma\ B_0 + n\omega_z \tag{10.7}$$

and for each n, directly from the amplitude in the phase-modulated rotating frame, the effective angular nutation frequency is

$$\omega_{nut} = \gamma\ B_{1,xy} J_n\left(\frac{\gamma B_{1,z}}{\omega_z}\right) \tag{10.8}$$

10.2 Multiphoton excitation with one $B_{1,xy}$ and two $B_{1,z}$ fields

In this case, $B_z = B_0 + B_{1,z1}\cos(\omega_{z1}t) + B_{1,z2}\cos(\omega_{z2}t)$ with a single $B_{1,xy}$ field. In our phase-modulated rotating frame, the effective fields are

$$B_{z,eff} = B_0 - \frac{\omega_{xy}}{\gamma} \tag{10.9}$$

$$B_{x,eff} = B_{1,xy}\cos\left(\frac{\gamma B_{1,z1}}{\omega_{z1}}\sin(\omega_{z1}t) + \frac{\gamma B_{1,z2}}{\omega_{z2}}\sin(\omega_{z2}t)\right) \tag{10.10}$$

$$B_{y,eff} = B_{1,xy}\sin\left(\frac{\gamma B_{1,z1}}{\omega_{z1}}\sin(\omega_{z1}t) + \frac{\gamma B_{1,z2}}{\omega_{z2}}\sin(\omega_{z2}t)\right) \tag{10.11}$$

Let $\alpha = \frac{\gamma B_{1,z1}}{\omega_{z1}}$ and $\beta = \frac{\gamma B_{1,z2}}{\omega_{z2}}$, Eqs. [10.10, 10.11] can be rewritten in complex notation as

$$B_{xy,eff} = B_{1,xy}\cos(\alpha\sin(\omega_{z1}t) + \beta\sin(\omega_{z2}t)) + iB_{1,xy}\sin(\alpha\sin(\omega_{z1}t) + \beta\sin(\omega_{z2}t)) \tag{10.12}$$

Or equivalently,

$$B_{xy,eff} = B_{1,xy}e^{i(\alpha\sin(\omega_{z1}t)+\beta\sin(\omega_{z2}t))} = B_{1,xy}e^{i\alpha\sin(\omega_{z1}t)}e^{i\beta\sin(\omega_{z2}t)} \tag{10.13}$$

Plugging Eq. [10.6] into Eq. [10.13] results in

$$B_{xy,eff} = B_{1,xy}\sum_{n=-\infty}^{\infty} J_n(\alpha)\, e^{in\omega_{z1}t}\sum_{m=-\infty}^{\infty} J_m(\beta)\, e^{im\omega_{z2}t} \tag{10.14}$$

$$B_{xy,eff} = \sum_{n=-\infty}^{\infty}\sum_{m=-\infty}^{\infty} B_{1,xy}J_n(\alpha)\, J_m(\beta)\, e^{i(n\omega_{z1}t+m\omega_{z2}t)} \tag{10.15}$$

Eq. [10.15] shows that in the phase-modulated rotating frame, xy-RF has angular frequencies of $n\omega_{z1}+m\omega_{z2}$. Thus, from Eqs. [10.9, 10.15], resonances occur whenever $\omega_{xy} = \gamma B_0 + n\omega_{z1} + m\omega_{z2}$, and the effective angular nutation frequency for n and m is

$$\omega_{nut} = \gamma\ B_{1,xy} J_n\left(\frac{\gamma B_{1,z1}}{\omega_{z1}}\right) J_m\left(\frac{\gamma B_{1,z2}}{\omega_{z2}}\right) \tag{10.16}$$

For more than two frequencies along the z-axis, the analysis straightforwardly extends to having more multiplied Bessel functions, one for each new frequency involved.

10.3 Variable Definitions

Variable	Definition
$M_x,\ M_y,\ M_z$	Magnetization vector components
M_0	Equilibrium magnetization
$B_x,\ B_y$	Transverse magnetic field vector components
B_0	Main static magnetic field strength
$T_1,\ T_2$	Longitudinal and transverse relaxation times
T	Duration of RF pulse
γ	Gyromagnetic ratio
m_{xy}	Transverse magnetization vector in complex notation
B_{xy}	Transverse magnetic field in complex notation
$B_{1,xy}$	Amplitude of transverse RF magnetic field
B_z	Total longitudinal magnetic field
$B_{1,z}$	Amplitude of longitudinal RF magnetic field
$B_{DC,z}$	Uniform near-DC longitudinal magnetic field
ω_0	Larmor frequency (γB_0)
ω_z	Longitudinal RF angular frequency
$\Delta\omega$	Shift in longitudinal RF angular frequency
ω_{xy}	Transverse RF angular frequency
ϕ	Longitudinal RF extra phase
θ	Transverse RF extra phase
$\mathbf{G}$	Gradient vector for spatial encoding
$\mathbf{G_{1,z}}$	Oscillating component of gradient vector for excitation
$\mathbf{k}$	Excitation k-space vector
$J_m(-)$	Bessel function of the first kind of order m

Table 10.1: Variable Definitions

Bibliography

[1] A. Abragam. *The Principles of Nuclear Magnetism*. en. Clarendon Press, 1961. ISBN: 978-0-19-852014-6.

[2] Caroline Andrews and Alyosha C. Molnar. "A Passive Mixer-First Receiver With Digitally Controlled and Widely Tunable RF Interface". In: *IEEE Journal of Solid-State Circuits* 45.12 (Dec. 2010). Conference Name: IEEE Journal of Solid-State Circuits, pp. 2696–2708. ISSN: 1558-173X. DOI: 10.1109/JSSC.2010.2077151.

[3] Caroline Andrews and Alyosha C. Molnar. "Implications of Passive Mixer Transparency for Impedance Matching and Noise Figure in Passive Mixer-First Receivers". In: *IEEE Transactions on Circuits and Systems I: Regular Papers* 57.12 (Dec. 2010). Conference Name: IEEE Transactions on Circuits and Systems I: Regular Papers, pp. 3092–3103. ISSN: 1558-0806. DOI: 10.1109/TCSI.2010.2052513.

[4] F. Bloch and A. Siegert. "Magnetic Resonance for Nonrotating Fields". In: *Physical Review* 57.6 (Mar. 15, 1940), pp. 522–527. DOI: 10.1103/PhysRev.57.522.

[5] R. Boscaino and G. Messina. "Double quantum coherent transients in a two-level spin system: A vectorial model". en. In: *Physica B+C* 138.1-2 (Mar. 1986), pp. 179–187. ISSN: 03784363. DOI: 10.1016/0378-4363(86)90506-1.

[6] Robert W. Boyd. *Nonlinear Optics*. English. 4th edition. Academic Press, July 31, 2020. ISBN: 978-0-323-85057-5.

[7] DO Brunner et al. "Sideband Excitation for Concurrent RF Transmission and Reception". In: ISMRM Annual Scientific Meeting & Exhibition. Montreal, Quebec, Canada, 2011.

[8] Jianshu Chi, Victor Han, and Chunlei Liu. "In vivo Two-photon Magnetic Resonance Imaging of Human Brain at 3T". In: *Proceedings of the ISMRM Annual Meeting and Exhibition* (2021), p. 0564.

[9] Leon W. Couch. *Digital & Analog Communication Systems*. English. 8 edition. Upper Saddle River, N.J: Pearson, Jan. 19, 2012. ISBN: 978-0-13-291538-0.

[10] G. R. Davies et al. "Continuous-Wave Magnetic Resonance Imaging of Short T2 Materials". In: *Journal of Magnetic Resonance* 148.2 (Feb. 1, 2001), pp. 289–297. ISSN: 1090-7807. DOI: 10.1006/jmre.2000.2245.

[11] P. T. Eles and C. A. Michal. "Two-photon excitation in nuclear magnetic and quadrupole resonance". In: *Progress in Nuclear Magnetic Resonance Spectroscopy* 56.3 (Apr. 1, 2010), pp. 232–246. ISSN: 0079-6565. DOI: 10.1016/j.pnmrs.2009.12.002.

[12] Philip T. Eles and Carl A. Michal. "Two-photon two-color nuclear magnetic resonance". In: *The Journal of Chemical Physics* 121.20 (Nov. 11, 2004), pp. 10167–10173. ISSN: 0021-9606. DOI: 10.1063/1.1808697.

[13] Koray Ertan et al. "A z-gradient array for simultaneous multi-slice excitation with a single-band RF pulse". en. In: *Magnetic Resonance in Medicine* 80.1 (2018), pp. 400–412. ISSN: 1522-2594. DOI: 10.1002/mrm.27031.

[14] Richard P. Feynman, Frank L. Vernon, and Robert W. Hellwarth. "Geometrical Representation of the Schrödinger Equation for Solving Maser Problems". In: *Journal of Applied Physics* 28.1 (Jan. 1, 1957), pp. 49–52. ISSN: 0021-8979. DOI: 10.1063/1.1722572.

[15] G. Goelman and J. S. Leigh. "Multiband Adiabatic Inversion Pulses". In: *Journal of Magnetic Resonance, Series A* 101.2 (Feb. 1, 1993), pp. 136–146. ISSN: 1064-1858. DOI: 10.1006/jmra.1993.1023.

[16] I Gromov and A Schweiger. "Multiphoton Resonances in Pulse EPR". en. In: *Journal of Magnetic Resonance* 146.1 (Sept. 1, 2000), pp. 110–121. ISSN: 1090-7807. DOI: 10.1006/jmre.2000.2143.

[17] Victor Han and Chunlei Liu. "Multiphoton magnetic resonance in imaging: A classical description and implementation". en. In: *Magnetic Resonance in Medicine* 84.3 (2020), pp. 1184–1197. ISSN: 1522-2594. DOI: https://doi.org/10.1002/mrm.28186. URL: https://onlinelibrary.wiley.com/doi/abs/10.1002/mrm.28186.

[18] M. E. Hayden, C. P. Bidinosti, and E. M. Chapple. "Specific absorption rates and signal-to-noise ratio limitations for MRI in very-low magnetic fields". en. In: *Concepts in Magnetic Resonance Part A* 40A.6 (2012), pp. 281–294. ISSN: 1552-5023. DOI: 10.1002/cmr.a.21247.

[19] D. I. Hoult and N. S. Ginsberg. "The Quantum Origins of the Free Induction Decay Signal and Spin Noise". en. In: *Journal of Magnetic Resonance* 148.1 (Jan. 1, 2001), pp. 182–199. ISSN: 1090-7807. DOI: 10.1006/jmre.2000.2229.

[20] Djaudat Idiyatullin et al. "Continuous SWIFT". In: *Journal of Magnetic Resonance* 220 (July 1, 2012), pp. 26–31. ISSN: 1090-7807. DOI: 10.1016/j.jmr.2012.04.016.

[21] Eric A.M. Klumperink, Hugo J. Westerveld, and Bram Nauta. "N-path filters and mixer-first receivers: A review". In: *2017 IEEE Custom Integrated Circuits Conference (CICC)*. ISSN: 2152-3630. Apr. 2017, pp. 1–8. DOI: 10.1109/CICC.2017.7993643.

[22] Peter J. Koopmans et al. "Simultaneous multislice inversion contrast imaging using power independent of the number of slices (PINS) and delays alternating with nutation for tailored excitation (DANTE) radio frequency pulses". en. In: *Magnetic Resonance in Medicine* 69.6 (2013), pp. 1670–1676. ISSN: 1522-2594. DOI: 10.1002/mrm.24402.

[23] Robert Kraus et al. *Ultra-Low Field Nuclear Magnetic Resonance: A New MRI Regime*. English. 1 edition. New York: Oxford University Press, Apr. 2, 2014. ISBN: 978-0-19-979643-4.

[24] D. J. Larkman et al. "Use of multicoil arrays for separation of signal from multiple slices simultaneously excited". eng. In: *Journal of magnetic resonance imaging: JMRI* 13.2 (Feb. 2001), pp. 313–317. ISSN: 1053-1807.

[25] P. C. Lauterbur. "Image Formation by Induced Local Interactions: Examples Employing Nuclear Magnetic Resonance". en. In: *Nature* 242.5394 (Mar. 1973), pp. 190–191. ISSN: 1476-4687. DOI: 10.1038/242190a0.

[26] Timo Liimatainen et al. "MRI contrast from relaxation along a fictitious field (RAFF)". en. In: *Magnetic Resonance in Medicine* 64.4 (2010), pp. 983–994. ISSN: 1522-2594. DOI: 10.1002/mrm.22372.

[27] Sebastian Littin et al. "Development and implementation of an 84-channel matrix gradient coil". en. In: *Magnetic Resonance in Medicine* 79.2 (2018), pp. 1181–1191. ISSN: 1522-2594. DOI: 10.1002/mrm.26700.

[28] J. Martin et al. "SigPy.RF: Comprehensive Open-Source RF Pulse Design Tools for Reproducible Research". In: *Proceedings of the ISMRM Annual Meeting and Exhibition* (2020), p. 1045.

[29] Craig H. Meyer et al. "Simultaneous spatial and spectral selective excitation". en. In: *Magnetic Resonance in Medicine* 15.2 (Aug. 1, 1990), pp. 287–304. ISSN: 1522-2594. DOI: 10.1002/mrm.1910150211.

[30] Carl A. Michal. "A low-cost spectrometer for NMR measurements in the Earth's magnetic field". en. In: *Measurement Science and Technology* 21.10 (Aug. 2010), p. 105902. ISSN: 0957-0233. DOI: 10.1088/0957-0233/21/10/105902.

[31] Carl A. Michal. "Nuclear magnetic resonance noise spectroscopy using two-photon excitation". In: *The Journal of Chemical Physics* 118.8 (Feb. 4, 2003), pp. 3451–3454. ISSN: 0021-9606. DOI: 10.1063/1.1553758.

[32] Ahmad Mirzaei et al. "Analysis and Optimization of Direct-Conversion Receivers With 25% Duty-Cycle Current-Driven Passive Mixers". In: *IEEE Transactions on Circuits and Systems I: Regular Papers* 57.9 (Sept. 2010). Conference Name: IEEE Transactions on Circuits and Systems I: Regular Papers, pp. 2353–2366. ISSN: 1558-0806. DOI: 10.1109/TCSI.2010.2043014.

[33] Karolinska University Hospital Neuro MR physics group. *KS Foundation – A platform for simpler EPIC programming*. [Online; accessed 2019-11-03]. URL: http://ksfoundationepic.org/index.html.

[34] Ali Caglar Özen et al. "In vivo MRI with Concurrent Excitation and Acquisition using Automated Active Analog Cancellation". En. In: *Scientific Reports* 8.1 (July 13, 2018), p. 10631. ISSN: 2045-2322. DOI: 10.1038/s41598-018-28894-w.

[35] J. Pauly et al. "Parameter relations for the Shinnar-Le Roux selective excitation pulse design algorithm (NMR imaging)". In: *IEEE Transactions on Medical Imaging* 10.1 (Mar. 1991), pp. 53–65. ISSN: 0278-0062. DOI: 10.1109/42.75611.

[36] John Pauly, Dwight Nishimura, and Albert Macovski. "A k-space analysis of small-tip-angle excitation". In: *Journal of Magnetic Resonance (1969)* 81.1 (Jan. 1, 1989), pp. 43–56. ISSN: 0022-2364. DOI: 10.1016/0022-2364(89)90265-5.

[37] Nathaniel J. Powell et al. "Gradient rotating outer volume excitation (GROOVE): A novel method for single-shot two-dimensional outer volume suppression". en. In: *Magnetic Resonance in Medicine* 73.1 (2015), pp. 139–149. ISSN: 1522-2594. DOI: 10.1002/mrm.25101.

[38] Norman F. Ramsey. "Resonance Transitions Induced by Perturbations at Two or More Different Frequencies". en. In: *Physical Review* 100.4 (Nov. 15, 1955), pp. 1191–1194. ISSN: 0031-899X. DOI: 10.1103/PhysRev.100.1191.

[39] Alexander P. Saiko, Ryhor Fedaruk, and Siarhei A. Markevich. "Multi-photon transitions and Rabi resonance in continuous wave EPR". In: *Journal of Magnetic Resonance* 259 (Oct. 1, 2015), pp. 47–55. ISSN: 1090-7807. DOI: 10.1016/j.jmr.2015.07.013.

[40] Klaus Scheffler et al. "Spread-spectrum magnetic resonance imaging". en. In: *Magnetic Resonance in Medicine* 82.3 (2019), pp. 877–885. ISSN: 1522-2594. DOI: 10.1002/mrm.27766.

[41] Kawin Setsompop et al. "Blipped-controlled aliasing in parallel imaging for simultaneous multislice echo planar imaging with reduced g-factor penalty". en. In: *Magnetic Resonance in Medicine* 67.5 (2012), pp. 1210–1224. ISSN: 1522-2594. DOI: 10.1002/mrm.23097.

[42] Sung-Min Sohn et al. "In Vivo MR Imaging with Simultaneous RF Transmission and Reception". In: *Magnetic resonance in medicine* 76.6 (Dec. 2016), pp. 1932–1938. ISSN: 0740-3194. DOI: 10.1002/mrm.26464.

[43] Trevelyan. *MRI and NMR Spectroscopy in the Earth's Field: Building a Low-Cost NMR Spectrometer for Hobby Science and Teaching*. en. Google-Books-ID: 6sFDyQEACAAJ. Independently Published, Apr. 17, 2019. ISBN: 978-1-09-378539-5.

[44] Pauli Virtanen et al. "SciPy 1.0: fundamental algorithms for scientific computing in Python". en. In: *Nature Methods* 17.3 (Mar. 2020), pp. 261–272. ISSN: 1548-7105. DOI: 10.1038/s41592-019-0686-2.

[45] Dmitriy A. Yablonskiy, Alexander L. Sukstanskii, and Joseph J. H. Ackerman. "Image artifacts in very low magnetic field MRI: The role of concomitant gradients". en. In: *Journal of Magnetic Resonance* 174.2 (June 1, 2005), pp. 279–286. ISSN: 1090-7807. DOI: 10.1016/j.jmr.2005.02.016.

[46] Y. Zur, M. H. Levitt, and S. Vega. "Multiphoton NMR spectroscopy on a spin system with $I = 1/2$". en. In: *The Journal of Chemical Physics* 78.9 (May 1983), pp. 5293–5310. ISSN: 0021-9606, 1089-7690. DOI: 10.1063/1.445483.